



The development and validation of a snow/icepack pavement temperature thermodynamic model
by Jeffrey Ryan Bristow

A thesis submitted in partial fulfillment of the requirements for the degree of Master of Science in Civil
Engineering

Montana State University

© Copyright by Jeffrey Ryan Bristow (2002)

Abstract:

A model was developed to predict the temperature and melting of snow and ice on roads for a single grid point with hopes to link the model with the Radiation Thermal Road Temperature Model (RadThermRT) and perform similar calculations over a large surface with many grid points. The model's geometry consists of two separate parts, the subgrade and the ice/snowpack. Sand, unbound rock aggregate, and bituminous asphalt are three materials used to represent a typical asphalt highway cross-section. At 1 meter down in the sub-grade a diurnal depth temperature is reached, which serves as the lower boundary condition for the model. The ice/snowpack is created using multiple 1 mm thick layers with specified properties such as, density (kg/m^3), impurity content (ppm), and grain size (mm). Air temperature (C), barometric pressure (mbar), relative humidity (%), incoming solar radiation (W/m^2), and cloud cover (%) are the meteorological inputs used to run the model. Each ice/snow layer has an albedo, which is calculated using the Computation Albedo Routine (CAR). Conduction, convection, short-wave radiation, long-wave radiation, and the latent heat of evaporation are heat transfer methods used to change the temperature or the phase of the ice and snow layers. In addition to temperature change and phase change a runoff function predicts how much time is needed for a melted layer of snow or ice to run off. Thermal energy balance is used to derive the differential equation solved in the model. The model is solved numerically using a variation of the Crank-Nicolson method to account for unequal mesh sizes. Absorbed solar radiation and impurity content play a large role in how much and where melt is going to occur in the snow and ice layers. An experiment was run to validate the model. Pure ice was modeled on a highway test box, providing assurance that the model was working correctly. Eight hypothetical experiments are also introduced to demonstrate the model's ability to account for snow versus ice and impurity content.

THE DEVELOPMENT AND VALIDATION OF A SNOW/ICEPACK
PAVEMENT TEMPERATURE THERMODYNAMIC MODEL

by

Jeffrey Ryan Bristow

A thesis submitted in partial fulfillment
of the requirements for the degree

of

Master of Science

in

Civil Engineering

MONTANA STATE UNIVERSITY – BOZEMAN
Bozeman, Montana

November 2002

© COPYRIGHT

by

Jeffrey Ryan Bristow

2002

All Rights Reserved

N378
B776

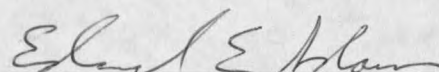
APPROVAL

of a thesis submitted by

Jeffrey Ryan Bristow

This thesis has been read by each member of the thesis committee and has been found to be satisfactory regarding content, English usage, format, citations, bibliographic style, and consistency, and is ready for submission to the College of Graduate Studies.


Dr. Edward E. Adams


(Signature)

25-NOV-2002
Date

Approved for the Department of Civil Engineering

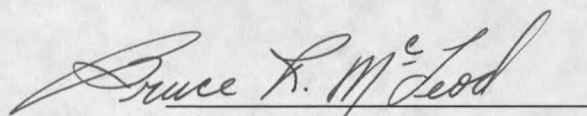
Dr. Brett Gunnink


(Signature)

25 Nov 2002
Date

Approved for the College of Graduate Studies

Dr. Bruce McLeod


(Signature)

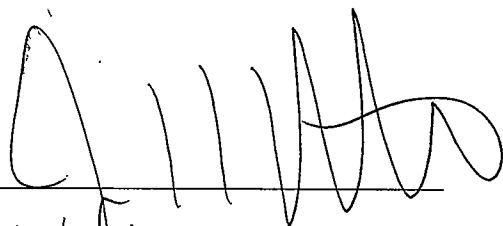
11-26-02
Date

STATEMENT OF PERMISSION TO USE

In presenting this thesis in partial fulfillment of the requirements for a master's degree at Montana State University – Bozeman, I agree that the library shall make it available to borrowers under rules of the Library.

If I have indicated my intention to copyright this thesis by including a copyright notice page, copying is allowable only for scholarly purposes, consistent with "fair use" as prescribed in the U.S. Copyright Law. Requests for permission for extended quotation from or reproduction of this thesis (paper) in whole or in parts may be granted only by the copyright holder.

Signature

A handwritten signature in black ink, consisting of a large initial 'A' followed by several vertical strokes and a final flourish.

Date

11/5/2002

TABLE OF CONTENTS

1. INTRODUCTION	1
2. BACKGROUND	5
THERMODYNAMICS AND TRANSPORT PHENOMENA	5
Heat Transfer	7
Conduction	7
Radiation	7
Turbulent Fluxes	9
Mass Transfer	9
Fluid Dynamics	10
WINTER MAINTENANCE OPERATIONS	11
Plowing	11
Abrasives	12
De-icers	13
Anti-icing	13
INPUT MODELS	14
CAR	14
RadThermRT	15
PREVIOUS ROAD/ICE TEMPERATURE MODELING	17
3. METHODOLOGY	21
THE MODEL	21
Steady State Heat Conduction	25
Long-wave Radiation	26
Saturation Vapor Pressures	27
Turbulent Fluxes	30
Solar Radiation	31
Energy Balance Equation	38
Phase Change	46
Runoff	49
USING THE MODEL'S MAIN INTERFACE	57
VALIDATION EXPERIMENT	59
4. FINDINGS/RESULTS	66
THE MODEL AND EXPERIMENTS	66
April 19, 2002	67

April 02, 2002.....	75
April 4, 2002.....	80
HYPOTHETICAL EXAMPLES.....	85
Case I.....	88
Case II.....	92
Case III.....	95
Case IV.....	99
Case V.....	100
Case VI.....	102
Case VII.....	106
Case VIII.....	108
Summary of Hypothetical Results.....	112
5. CONCLUSIONS AND RECOMMENDATIONS.....	113
REFERENCES.....	118
APPENDICES.....	123
APPENDIX A: MATLAB CODE LISTING FOR THE MODEL.....	124
APPENDIX B: C++ CODE LISTING FOR THE COMPUTATIONAL ALBEDO ROUTINE.....	153

LIST OF TABLES

Table	Page
1. 1999 fatalities in Wyoming, Idaho, and Montana (reproduced from table 1 p. 2 Ballard 2001).	6
2. Physical properties of the road sub-grade.	22
3. The extinction coefficients for pure bubble free ice in the visible range (400-700 nm), (reproduced from table 1 page 7449 Grenfell and Perovich 1981).	32
4. Absorption coefficient calculations for both soot and dust using Equation (24).....	35
5. The albedo's for each layer that CAR generated and the adjusted albedo's used for generating results in Figure 20.....	71

LIST OF FIGURES

Figure	Page
1. Greater Yellowstone Corridor.....	6
2. The heating curve for ice. (reproduced from figure 19-6 p. 451 Hudson and Nelson 1990).....	10
3. Flow chart of how the three models interact.....	17
4. Geometry and node spacing for the model.	23
5. Temperature fluctuations vs. time at the Fort Assiniboine site. (a) presents all five of the soil depths (b) presents the 1 m depth with the sinusoidal curve.....	24
6. The imaginary part of the refractive index for soot and dust. (reproduced from Figure 8, page 10,227 Aoki 2000). [The square boxes represent the imaginary part of the refractive index for dust and soot in the visible wavelengths].....	35
7. Graphical representation of the algorithm used to estimate absorbed solar radiation. [Bold labels next to arrows represent absorbed radiation in the layer].....	38
8. Schematic drawing of one layer used in the derivation of the transient heat conduction differential equation.	40
9. The unequal mesh used to find the solution technique to solve the second order differential equation.....	43
10. Graphical representation of where the δs was located in a melting layer.....	47
11. Velocity profiles calculated using the Navier-Stokes equation for confined flow and the calculation for the average runoff time. (a) for a 2% road grade (b) for a 3% road grade.	53
12. Drawing used for the flow of a falling film velocity. (a) shows where the unconfined layer is. (b) a blow up of the top layer and the shell boundary.....	54
13. Sample code in the main program. (a) sample code for meltall = yes (b) sample code for metal = no and the a_p is defined.....	59

14. Test box used for the validation experiment.....	60
15. Map of Bozeman, MT and the location of the test site.....	61
16. Drawing of the insulated bowl used when making pure ice.	63
17. Picture of the WEATHERPAK-400 and the Li-Cor pyranometer at the test site. [The Li-Cor pyranometer is mounted on the horizontal bar].....	65
18. Plots created during the validation experiment on April 19, 2002. (a) temperature vs. time for six thermocouples used in the experiment. (b) measured solar radiation vs. time.....	69
19. Model results for April 19, 2002. (a) sub-grade profile depth vs. temperature plotted every ten minutes. (b) number of ice layers vs. time. (c) pavement surface temperature vs. time.	70
20. Model results for April 19, 2002 with adjusted albedo's. (a) sub-grade profile depth vs. temperature plotted every ten minutes. (b) number of layers vs. time. (c) pavement surface temperature vs. time.....	72
21. Plots of both the measured and the model's predicted asphalt surface temperature vs. time for the April 19, 2002 experiment.....	74
22. Values of measured thickness of ice above the asphalt surface during the experiment, and a plot of both measured and predicted thickness of ice above the asphalt surface vs. time for the April 19, 2002 experiment.....	74
23. Plots created during the validation experiment on April 2, 2002. (a) temperature vs. time for six thermocouples used in the experiment. (b) measured solar radiation vs. time.....	77
24. Model results for April 02, 2002 with adjusted albedo's. (a) sub-grade profile depth vs. temperature plotted every ten minutes. (b) number of ice layers vs. time. (c) pavement surface temperature and ice surface temperature vs. time.....	78
25. Model results for April 02, 2002 with adjusted albedo's and a sand layer added. (a) sub-grade profile depth vs. temperature plotted every ten minutes. (b) number of ice layers vs. time. (c) pavement surface temperature and ice surface temperature vs. time.	80
26. Plots created during the validation experiment on April 4, 2002. (a) temperature vs. time for six thermocouples used in the experiment. (b) measured solar radiation vs. time.	82

27. Model results for April 04, 2002 with adjusted albedo's. (a) sub-grade profile depth vs. temperature plotted every ten minutes. (b) number of ice layers vs. time. (c) pavement surface temperature vs. time.83
28. Plots of both the measured and the model's predicted asphalt surface temperature vs. time for the April 04, 2002 experiment.84
29. Values of measured thickness of ice above the asphalt surface during the experiment, and a plot of both measured and predicted thickness of ice above the asphalt surface vs. time for the April 04, 2002 experiment.84
30. Plots of weather conditions created for the 8 hypothetical examples. (a) air temperature vs. time. (b) solar radiation vs. time. (c) cloud cover vs. time.86
31. General plots to show how much and where the turbulent and long-wave radiation fluxes are accounted for. (a) convection vs. time absorbed only at the top surface of snow or ice. (b) long-wave radiation vs. time absorbed at the top two layers of the snow or ice.88
32. Profiles created to show the ice layer properties for case I, α is the layer albedo and ρ is the layer density. (a) ice layer properties used for inputs I the model. (b) the order of the melting ice layers. (c) final ice properties after the model was run. A solid line denotes each layer and a dotted line represents a layer that has melted. Numbers are used to express the order of layer runoff.89
33. Graphs of general results for the hypothetical example: Case I. (a) sub-grade profile depth vs. temperature plotted every ten minutes. (b) number of ice layers above the pavement surface vs. time. (c) pavement surface temperature and ice surface temperatures vs. time.90
34. Graphs of layer results for hypothetical example: Case I. (a) top ice layer temperature profile vs. time. (b) absorbed solar radiation at the top ice layer vs. time. (c) ice layer 11 temperature profile vs. time. (d) absorbed solar radiation at ice layer 11 vs. time. (e) ice layer 3 temperature profile vs. time. (f) absorbed solar radiation at ice layer 3 vs. time. (g) asphalt surface temperature profile vs. time. (h) absorbed solar radiation at the asphalt surface vs. time.91
35. Profiles created to show the snow layer properties for case II, α is the layer albedo and ρ is the layer density. (a) snow layer properties used for inputs in the model. (b) the order of the melting snow layers. (c) final snow properties after the model was run. A solid line denotes each layer and a dotted line represents a layer that has melted. Numbers are used to express the order of layer runoff.93

36. Graphs of general results for the hypothetical example: Case II. (a) sub-grade profile depth vs. temperature plotted every ten minutes. (b) number of snow layers above the pavement surface vs. time. (c) pavement surface temperature and snow surface temperatures vs. time.94

37. Graphs of layer results for hypothetical example: Case II. (a) top snow layer temperature profile vs. time. (b) absorbed solar radiation at the top snow layer vs. time. (c) snow layer 6 temperature profile vs. time. (d) absorbed solar radiation at snow layer 6 vs. time. (e) temperature profile vs. time at the asphalt surface. (f) absorbed solar radiation vs. time at the asphalt surface.95

38. Profiles created to show the ice layer properties for case III, α is the layer albedo and ρ is the layer density. (a) ice layer properties used for inputs in the model. (b) the order of the melting ice layers. (c) final ice properties after the model was run. A solid line denotes each layer and a dotted line represents a layer that has melted. Numbers are used to express the order of layer runoff.....96

39. Graphs of general results for the hypothetical example: Case III. (a) sub-grade profile depth vs. temperature plotted every ten minutes. (b) number of ice layers above the pavement surface vs. time. (c) pavement surface temperature and ice surface temperatures vs. time.97

40. Graphs of layer results for hypothetical example: Case III. (a) top ice layer temperature profile vs. time. (b) absorbed solar radiation at the top ice layer vs. time. (c) ice layer 12 temperature profile vs. time. (d) absorbed solar radiation at ice layer 12 vs. time. (e) ice layer 7 temperature profile vs. time. (f) absorbed solar radiation at ice layer 7 vs. time. (g) asphalt surface temperature profile vs. time. (h) absorbed solar radiation at the asphalt surface vs. time.98

41. Profiles created to show the ice layer properties for case IV, α is the layer albedo and ρ is the layer density. (a) ice layer properties used for inputs in the model. (b) the order of the melting ice layers. (c) final ice properties after the model was run. A solid line denotes each layer and a dotted line represents a layer that has melted. Numbers are used to express the order of layer runoff.....99

42. Graphs of general results for the hypothetical example: Case IV. (a) sub-grade profile depth vs. temperature plotted every ten minutes. (b) number of ice layers above the pavement surface vs. time. (c) pavement surface temperature and ice surface temperatures vs. time.100

43. Profiles created to show the ice layer properties for case V, α is the layer albedo and ρ is the layer density. (a) ice layer properties used for inputs in the model. (b) the order of the melting ice layers. (c) final ice properties after the model was run. A solid line denotes each layer and a dotted line represents a layer that has melted. Numbers are used to express the order of layer runoff.....101
44. Graphs of general results for the hypothetical example: Case V. (a) sub-grade profile depth vs. temperature plotted every ten minutes. (b) number of ice layers above the pavement surface vs. time. (c) pavement surface temperature and ice surface temperatures vs. time.102
45. Profiles created to show the snow layer properties for case VI, α is the layer albedo and ρ is the layer density. (a) snow layer properties used for inputs in the model. (b) the order of the melting snow layers. (c) final snow properties after the model was run. A solid line denotes each layer and a dotted line represents a layer that has melted. Numbers are used to express the order of layer runoff.....103
46. Graphs of general results for the hypothetical example: Case VI. (a) sub-grade profile depth vs. temperature plotted every ten minutes. (b) number of snow layers above the pavement surface vs. time. (c) pavement surface temperature and snow surface temperatures vs. time.104
47. Graphs of layer results for hypothetical example: Case VI. (a) top snow layer temperature profile vs. time. (b) absorbed solar radiation at the top snow layer vs. time. (c) snow layer 12 temperature profile vs. time. (d) absorbed solar radiation at snow layer 12 vs. time. (e) ice layer 8 temperature profile vs. time. (f) absorbed solar radiation at snow layer 8 vs. time. (g) asphalt surface temperature profile vs. time. (h) absorbed solar radiation at the asphalt surface vs. time.105
48. Profiles created to show the snow layer properties for case VII, α is the layer albedo and ρ is the layer density. (a) snow layer properties used for inputs in the model. (b) the order of the melting snow layers. (c) final snow properties after the model was run. A solid line denotes each layer and a dotted line represents a layer that has melted. Numbers are used to express the order of layer runoff.....106
49. Graphs of general results for the hypothetical example: Case VII. (a) sub-grade profile depth vs. temperature plotted every ten minutes. (b) number of snow layers above the pavement surface vs. time. (c) pavement surface temperature and snow surface temperatures vs. time.107

50. Profiles created to show the snow layer properties for case VIII, α is the layer albedo and ρ is the layer density. (a) snow layer properties used for inputs in the model. (b) the order of the melting snow layers. (c) final snow properties after the model was run. A solid line denotes each layer and a dotted line represents a layer that has melted. Numbers are used to express the order of layer runoff.....108
51. Graphs of general results for the hypothetical example: Case VIII. (a) sub-grade profile depth vs. temperature plotted every ten minutes. (b) number of snow layers above the pavement surface vs. time. (c) pavement surface temperature and snow surface temperatures vs. time.110
52. Graphs of layer results for hypothetical example: Case VIII. (a) snow layer 14 temperature profile vs. time. (b) absorbed solar radiation at snow layer 14 vs. time. (c) snow layer 11 temperature profile vs. time. (d) absorbed solar radiation at snow layer 11 vs. time. (e) ice layer 2 temperature profile vs. time. (f) absorbed solar radiation at snow layer 2 vs. time. (g) asphalt surface temperature profile vs. time. (h) absorbed solar radiation at the asphalt surface vs. time.111

NOMENCLATURE

- A Area (m^2).
- A_{imp} Amount of impurities (ppm).
- AGW Aggregate weight (g).
- B_x Body force (m/s^2).
- cc Cloud cover fraction (%).
- C_p Specific heat (J/kg-K).
- ds Amount of melt (mm).
- dy Thickness of a snow/ice layer (mm).
- D_{oyr} Day of the year.
- e_a Air water vapor pressure (kPa).
- e_s Surface water vapor pressure (kPa).
- ED Effective depth (m).
- h_l Enthalpy of liquid water at 0°C (kJ/kg).
- h_s Enthalpy of solid water at 0°C (kJ/kg).
- g Gravitation acceleration (m/s^2).
- I Available short-wave radiation (W/m^2).
- I_a Absorbed short-wave radiation flux (W/m^2).
- I_o Initial short-wave radiation flux (W/m^2).
- I_r Reflective short-wave radiation flux (W/m^2).
- I_t Transmitted short-wave radiation flux (W/m^2).

- I_{tot_a} Total absorbed short-wave radiation flux (W/m^2).
- κ Thermal conductivity ($W/m\cdot K$).
- k Absorption coefficient ($1/m$).
- $K_{h,e}$ Dimensionless turbulent heat transfer coefficient.
- L_e Latent heat of water vaporization (kJ/kg).
- L_f Latent heat of fusion (kJ/kg).
- m_{im} Imaginary complex refractive index.
- n Top layer of snow/ice.
- P_{atm} Atmospheric pressure (mbar).
- $q_{con(y)}$ Heat conduction into a layer in the y direction (W/m^2).
- q_l Heat source flux associate with latent heat (W/m^2).
- q_s Heat source flux associate with turbulent and radiation fluxes (W/m^2).
- q_y Steady state conduction in the y direction (W/m^2).
- $Q_{con(y)}$ Net conduction energy in the y direction (J).
- Q_e Latent heat flux (W/m^2).
- Q_g Energy generation (J).
- Q_h Convection heat flux (W/m^2).
- Q_l Energy generated due to latent heat (J).
- Q_{lw} Long-wave radiation flux (W/m^2).
- Q_s Energy generated due to heat source terms (J).
- Q_{sw} Short-wave radiation flux (W/m^2).
- R Gas constant ($kJ/kg\cdot K$).

RH	Relative humidity (%).
s	Entropy (kJ/kg-K).
t_{runoff}	Time for runoff (s).
T_{air}	Air temperature ($^{\circ}C$).
T_g	Diurnal depth temperature ($^{\circ}C$).
T_s	Surface temperature ($^{\circ}C$).
T_{top}	Temperature of the top layer ($^{\circ}C$).
TW	Total weight (g).
u	Velocity in the x direction (m/s).
U	Internal energy (kJ/kg).
U_c	Velocity for a confined flow (m/s).
U_f	Velocity for a falling film flow (m/s).
v	Velocity in the y direction (m/s).
V_w	Wind velocity (m/s).
w	Velocity in the z direction (m/s).
W	Mechanical work (J).
x,y,z	Cartesian coordinates.
α	Albedo.
α_{total}	Albedo.
β	Attenuation coefficient (1/m).
ΔE	Change in energy during phase change (W/m^2).
ΔE_s	Change in energy stored (J).

Δy	Thickness of the unconfined layer (mm).
ε_s	Emissivity of snow.
λ	Wavelength (m).
μ	Viscosity of water (Ns/m ²).
τ_{ij}	Momentum flux on the i-face in the j-direction (kg/m-s).
θ	Slope of the road (°).
ν	Specific volume (m ³ /kg).
Φ_{ij}	Rate of momentum flux on the i-face in the j-direction (kg/s).
ρ	Density (kg/m ³).
σ	Stefen-Boltzmann constant (W/m ² -K ⁴).

ABSTRACT

A model was developed to predict the temperature and melting of snow and ice on roads for a single grid point with hopes to link the model with the Radiation Thermal Road Temperature Model (RadThermRT) and perform similar calculations over a large surface with many grid points. The model's geometry consists of two separate parts, the sub-grade and the ice/snowpack. Sand, unbound rock aggregate, and bituminous asphalt are three materials used to represent a typical asphalt highway cross-section. At 1 meter down in the sub-grade a diurnal depth temperature is reached, which serves as the lower boundary condition for the model. The ice/snowpack is created using multiple 1 mm thick layers with specified properties such as, density (kg/m^3), impurity content (ppm), and grain size (mm). Air temperature (C), barometric pressure (mbar), relative humidity (%), incoming solar radiation (W/m^2), and cloud cover (%) are the meteorological inputs used to run the model. Each ice/snow layer has an albedo, which is calculated using the Computation Albedo Routine (CAR). Conduction, convection, short-wave radiation, long-wave radiation, and the latent heat of evaporation are heat transfer methods used to change the temperature or the phase of the ice and snow layers. In addition to temperature change and phase change a runoff function predicts how much time is needed for a melted layer of snow or ice to run off. Thermal energy balance is used to derive the differential equation solved in the model. The model is solved numerically using a variation of the Crank-Nicolson method to account for unequal mesh sizes. Absorbed solar radiation and impurity content play a large role in how much and where melt is going to occur in the snow and ice layers. An experiment was run to validate the model. Pure ice was modeled on a highway test box, providing assurance that the model was working correctly. Eight hypothetical experiments are also introduced to demonstrate the model's ability to account for snow versus ice and impurity content.

CHAPTER 1

INTRODUCTION

During the winter months the northern United States and many other countries throughout the world suffer frequent snowfall and icy roads. This extreme weather leads to dangerous traveling conditions [Shao 1998]. As the United States and the rest of the world become more populated, the need for safer transportation will be even more of an issue than in the past. New proactive technologies that are being used today are anti-icing, roadway weather information systems (RWIS), thermal mapping, and the use of new and more sophisticated weather prediction models [Nixon 2001]. Accurate numerical prediction of road surface temperature has been proven to help save money and reduce accidents and is accepted as a viable method in the industry. These numerical predictions have demonstrated in dropping the cost of winter road maintenance [Shao and Lister 1996].

In Wisconsin the use of a winter weather system that includes a remote automatic roadside weather station and a numerical road ice prediction model has reduced the salt usage by 2500 tons and saved \$75,500 during a single winter storm [Stephenson 1988]. A survey commissioned by the UK Meteorological Office shows that approximately \$272M and 25-50 lives have been saved every year with the road ice prediction system in the UK [Thornes 1994]. These numbers will increase with more accurate meteorological and numerical road ice prediction models.

With the ability to predict when and where melting is going to occur, winter maintenance agencies will be able to more effectively and efficiently keep roads snow and ice free, allowing motorists, commercial services, and emergency vehicles to get to their destination faster and safer. Road ice prediction models can also help reduce excessive abrasive and chemical application, which leads to pollution of our environment [Nixon 2001].

A model for road snow/ice/water phase transformation will be developed, explained, and validated throughout this thesis. This model can prove to be very useful in a winter operation-forecasting environment. Models for balance of energy and mass are comparable to those developed by Ishikawa et al. [1999], Sass [1992], and Shao and Lister [1996]. The model is similar to other models in that it uses an energy balance taking into account sensible, radiative, latent heat fluxes, and ground conduction. The model extends the analysis by accounting for melting and runoff, also including an in depth look at how short-wave (solar) radiation is absorbed and is reflected in the snow/icepack.

Narsue et al. [1987] found absorbed short-wave radiation to be the dominant controlling factor of the ablation process and the change in snow properties. Monitoring of solar radiation and albedo was recommended for predicting ablation processes on the road. Albedo is the ratio of reflected radiation to the incident radiation [Gray and Male 1981, Marshall 1989, Wiscombe and Warren 1980a]. Although albedo will be explained, for a more detailed understanding of albedo and the optical properties of snow refer to Beddoe [2001], Marshall [1989], and Wiscombe and Warren [1980a and 1980b].

As albedo decreases, the snowpack absorbs a larger percentage of solar radiation. The more solar radiation that is absorbed provides, the greater the potential for increasing the temperature and inducing melting of the snow and ice. Impurities in the snow and ice such as carbon soot, continental dust, and volcanic ash decrease the snow's albedo, in turn increasing the amount of short-wave radiation that is absorbed [Choudhury 1981, Warren 1984, Wiscombe and Warren 1980b]. When albedo is decreased due to the addition of contaminants, an increase in absorbed solar radiation is expected. Because carbon soot is highly absorptive, about five to eight orders of magnitude greater than pure ice [Choudhury 1981], small amounts of soot will greatly increase the amount of solar radiation absorbed by the snowpack. Impurity content and distribution is very important in the model when trying to predict where melt is going to occur.

This model is one part of what will eventually be a three-part system used to model the thermodynamic properties of ice and snow on highways. The other two models are the Radiation Thermal Road Temperature Model (RadThermRT) and the computational albedo routine. At this time, input files are created to simulate RadThermRT's output and RadThermRT will eventually be linked with this model. Although RadThermRT and the computational albedo routine provide the major inputs into this model they will not be developed and only touched on briefly, for more literature on RadThermRT or the computational albedo routine see ThermoAnalytics [2000], and Beddoe [2001].

The model presented is a one-dimensional model with a lower boundary at a diurnal depth (i.e. a depth where fluctuations in temperature throughout a given day are approximately constant), taken as one meter in this analysis, continuing up through the

pavement to the snow/ice air interface. A version of the basic energy equation with heat sources (e.g. radiation, sensible, and latent heat) constitutes the underlying differential equation for this model. The model is broken into numerous unequal sized layers and solved using a variation of the Crank-Nicolson finite difference method (see chapter 3) [Gerald and Wheatly 1994, Ozisik 1993].

Inputs into the model were designed to be fairly simple so a forecaster and weather forecasting model combination could be used. There are two types of inputs: one is meteorological and the second includes snow parameters. The meteorological inputs are day of the year, cloud cover, air temperature, solar radiation, barometric pressure, relative humidity, long-wave radiation, and wind speed. These inputs are outputs provided by RWIS stations in the USA [Nixon 2001]. The snow parameters are the number of 1 mm layers, layer density, impurity content, initial surface temperature, and the albedo of each layer. The albedo of each layer comes directly from the computational albedo routine.

The theoretical mathematical model was experimentally validated. The validation experiment proved to be successful in providing temperature profiles similar to the profiles created by the model. It also provided the author with a better understanding of the problem being solved. Chapters 3, 4, and 5 address the validation experiment.

CHAPTER 2

BACKGROUND

The Greater Yellowstone Regional Traveler and Weather Information System (GYRTWIS), a project taken on by the Western Transportation Institute (WTI) and Montana State University, provided the necessary support for this research. The GYRTWIS project was created to help improve weather measurements, forecasts, and dissemination of such information in the Greater Yellowstone region. The scenic beauty, abundant wildlife and intriguing natural history draws over three million people to annually visit the Greater Yellowstone region (Figure 1). The mountainous terrain and highly variable winter weather conditions make traveling in the Greater Yellowstone region potentially dangerous. Fatality statistics from 1999 show that 20% of the fatalities that occur in the Greater Yellowstone region happened because of either adverse weather or adverse road conditions (Table 1) [NHTSA 2000]. A part of the GYRTWIS project includes the development of a pavement thermal model. The research presented here is intended to be incorporated into the pavement thermal model.

Thermodynamics and Transport Phenomena

The principles of Thermodynamics are based on the observations of physical phenomena [Black and Hartley 1996]. Thermodynamics is the study of energy and its relationship with the properties of matter. Black and Hartley [1996] simply define energy as the capacity to produce change. In the present study, changes in temperature, phase,

and/or the movement of fluid are of primary interest. Concepts of heat transfer, mass transfer, fluid dynamics, and how they influence the melting and freezing of snow and ice on pavement are discussed in detail in the following sections.

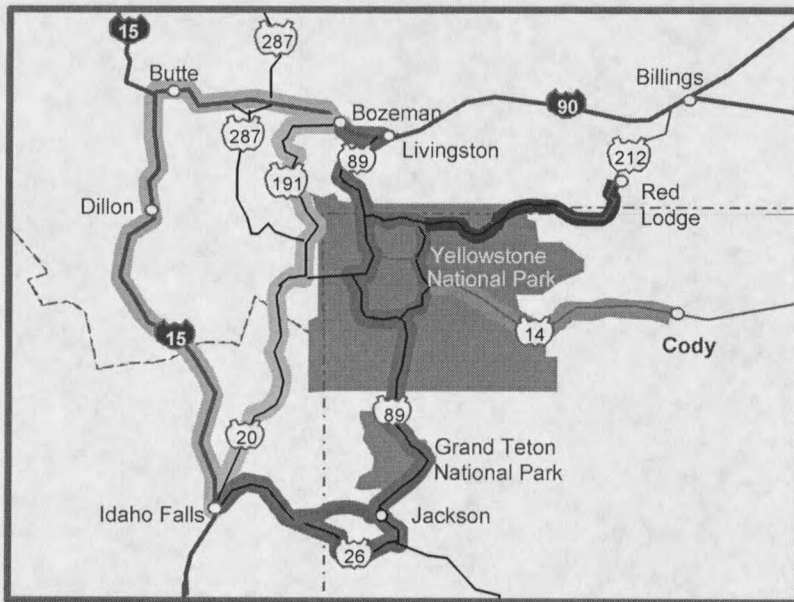


Figure 1. Greater Yellowstone Corridor.

Table 1. 1999 fatalities in Wyoming, Idaho, and Montana (reproduced from table 1 p. 2 Ballard 2001).

Road Condition	Dry	Wet	Snow or Slush	Ice	Sand, Dirt, Oil	Other	Unknown	Total
Atmospheric Condition								
No Adverse Atmospheric Conditions	543	17	7	35	2	6	2	612
Rain	1	24	0	3	0	0	0	28
Sleet(Hail)	0	1	2	0	0	0	0	3
Snow	0	6	9	16	0	0	0	31
Fog	1	2	0	0	0	0	0	3
Other(Smog, Smoke, Blowing Sand or Dust)	6	0	0	1	0	0	1	8
Unknown	1	0	0	0	0	1	0	2
Total	552	50	18	55	2	7	3	687

Heat Transfer

Heat transfer can be defined as: methods that energy can be transferred by interactions of a system with its surroundings [Incropera and DeWitt 1996]. The important methods of heat transfer for the model are conduction, long-wave radiation, short-wave radiation, sensible, and latent heat of phase change.

Conduction. The definition of conduction is an exchange of energy by direct interaction between molecules of a substance containing a temperature difference [White 1991]. When energy is transferred by conduction it will occur in the direction of decreasing temperature. In winter, the temperature in the sub-grade typically decreases from the diurnal depth to the pavement surface, providing the surface with energy that will increase the temperature or change the phase of the snow and ice. In some instances the sub-grade temperatures can be lower than the snow or ice, causing conductive heat flow in the other direction, cooling the snow or ice at the surface.

Radiation. Radiation is a transfer of energy in the form of electromagnetic waves. For this study the electromagnetic waves are emitted and absorbed at the pavement surface, in the snow/icepack, and at the snow/ice surface. Radiation in this study is broken into two parts, short-wave and long-wave. Thermal pavement model is concerned with both types of radiant energy.

Long-wave Radiation. Long-wave radiation is emitted by the earth and atmosphere and has wavelengths of 4000 to 100000 nm [Gray and Male 1981]. According to the law

of Stefan and Boltzman any body with a temperature greater than 0 K emits radiation. Incoming long-wave radiation is radiation that is emitted by the atmosphere. The greenhouse of the earth (e.g. water vapor, carbon dioxide, and ozone) is the main emitter of incoming long-wave radiation [Pluss 1997]. Long-wave radiation is driven by the temperature difference between the atmosphere and the earth's surface. On clear days the atmosphere is much cooler than the earth's surface, therefore pulling energy from the surface. This extraction of energy plays a major role in cooling the ice/snow surface. On occasion, clouds can be warmer than the surface, causing an inversion, and that can instead actually supply the earth's surface with energy via long-wave radiation.

Short-wave Radiation. The radiant energy from the sun is the primary source of energy forcing atmospheric motion and many different processes in the atmosphere, in the oceans and at the earth's surface [Pluss 1997]. Short-wave (solar) radiation emitted by the sun in wavelengths of 200 to 4000 nm accounts for more than 99% of the energy received from the sun at the top of the atmosphere. Short-wave radiation can yet be broken down into three more general categories depending on wavelength; 200-400 nm ultraviolet, 400-750 nm visible, and 750-4000 nm near infrared [Pluss 1997]. Less than 0.1% of the total short-wave radiation that arrives at the earth's surface is below 300 nm due to absorption by stratospheric ozone [Marshall 1989]. Leaving visible and near infrared radiation as the biggest contributors to the heating and melting of ice and snow. Small amounts of impurities (e.g. carbon soot, volcanic ash, dust, etc.) in pure snow/ice can drastically change how solar radiation is absorbed or reflected. According to Wiscombe and Warren [1980b] concentrations of 1 part per million by weight (ppmw)

can lower snow albedo by 5-15% from high values of 96-99%. As mentioned earlier, lowering the albedo allows more solar radiation to be transmitted or absorbed in the snowpack.

Turbulent Fluxes. The latent heat of evaporation, sublimation, and condensation is the internal energy associated with the phase change of the system [Cengel and Boles 1994]. When compared to radiation, the convective flux and the latent heat flux are often relatively small but still play a role in cooling or warming the snow surface. Convection, sometimes known as sensible heat, is the exchange of energy between a solid (ice/snow) and an adjacent liquid or gas (air) which is in motion [Cengel and Boles 1994]. This process is affected by wind speed and air temperature.

Mass Transfer.

Water is the only substance that occurs naturally on earth in all three phases (e.g. solid, liquid, and vapor) [Hudson and Nelson 1990]. Phase change is a process where by the physical characteristics of the substance are altered without a change in temperature. When dealing with snow/ice on the highways all three phases of water are present. For water, the phase change temperature from solid to liquid is 0° C and for changing from liquid to vapor the temperature is 100° C at standard pressure. A simple example of phase change is a block of ice at a temperature below its freezing point (0° C). When heat is added the block will increase in temperature until the surface of the block has reached its melting point. At this stage the block will still be absorbing energy but not changing temperature, all the energy is going into changing the phase of the block. After

the block has melted completely into water, the continued addition of heat will eventually rise in temperature until it reaches its boiling point (100°C). At this point again, the temperature will not change until all the liquid has vaporized into steam. Finally, the steam will again rise in temperature as heat is added (Figure 2).

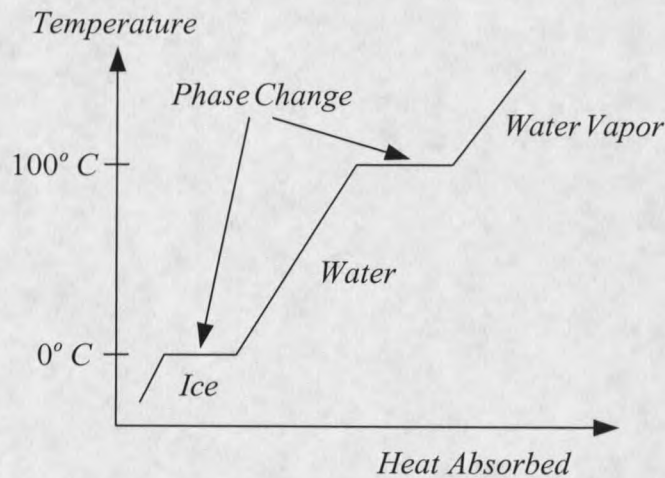


Figure 2. The heating curve for ice. (reproduced from figure 19-6 p. 451 Hudson and Nelson 1990).

Fluid Dynamics.

Representation of heat and mass transfer phenomena is imperative for modeling how the physical properties of the ice/snow are going to change temperature and phase. Heat and mass transfer constitute two of the three transport phenomena, the other is fluid dynamics. Although fluid flow is a form of mass transfer, in this paper, phase change will be categorized as mass transfer and fluid dynamics will imply the movement of the fluid. When the snow/ice is in the liquid phase one should expect fluid movement on an

unconfined surface (e.g. road surface). Highways and roads are designed to slope with the highest point in the middle, so rain will runoff to the side instead of puddling in the road, causing dangerous driving conditions [Huang 1993]. Runoff is a necessary component of the model to be presented.

Winter Maintenance Operations

Winter maintenance operations are becoming more reliant on scientific methods and technologies. Reactive methods (i.e. plowing, abrasives, and de-icing) are still major a part of winter maintenance, but winter agencies are starting to adopt new methods for keeping the roads snow and ice free. Winter maintenance operations are getting into more proactive methods such as anti-icing and thermal modeling [Nixon 2001]. A proactive method implies fighting the snow before it has had the chance to freeze to the road. The effectiveness of snow removal is highly dependent upon the physical properties of the snow (e.g. density, strength of snow pavement bond, liquid water content, amount of snow, etc.) [Beddoe 2001].

Plowing.

Plowing is still the primary method used for snow removal. The purpose of plowing is to move the material from one place (the road) to another (the ditch). There are five types of plows that are the most popular, front plows, underbody plows, wing plows, rotary plows, and power brooms [Gray and Male 1981]. Front plows, wing plows, and underbody plows are all forms of displacement plows with the intent of pushing the snow

off the road. Rotary plows and power brooms are large snow blowers that cut through the snow, essentially fluidizing the snow, and then blow it to the side of the road. Rotary plows operate at a much lower speed than front plows, wing plows, or underbody plows. Plowing, although being very effective can also be dangerous for the driver and others. Depending on the amount of snow on the road plow drivers need to maintain a minimum speed to get the snow to the side of the road. Sometimes these speeds can exceed 45 miles per hour (mph) causing blowing of snow and reduced visibility [Nixon 2001]. A 15-ton vehicle traveling at 45 mph with limited visibility has the potential of causing a serious accident and poses significant danger.

Abrasives.

Abrasives are used to increase the friction or decrease stopping distances on the road. When stopping distance is unknown and variable drivers tend to leave too much distance in front of them. This affects headway and restricts the number of vehicles on the road causing backup and slow moving traffic. A good abrasive will have resistance to crushing so it does not degrade in traffic, an angular shape so it will not blow away and provide good friction, a darkish color to help radiation absorption, and a uniform grain size so it does not clog the spreaders [Gray and Male 1981]. Often abrasives are pre-wetted with Calcium Chloride (CaCl_2) or Sodium Chloride (NaCl) to avoid water freezing and clumping during storage. They also help seed the abrasive into the snow/ice upon application, and help the abrasive stick to the road. 96% of the pre-wetted abrasives stick to the road opposed to 70% when not pre-wetted [Nixon 2001]. Since abrasives are

dark in color they lower the albedo of the snow/ice causing more solar radiation to be absorbed.

De-icers.

De-icers are chemicals that are spread onto the snow/ice covered road to melt into the ice and break the ice/pavement bond. De-icers are not used to melt all the snow and ice above the road. Some qualities of a good de-icer are the following: low eutectic temperature, exothermic process, easy and safe for handling, safe for the environment, minimal corrosive properties, effective melting rate, available in bulk quantity, and low in cost [Gray and Male 1981]. Two of the most popular de-icers used today are CaCl_2 and NaCl .

Anti-icing.

Anti-icing is a strategy whereby chemicals are applied prior to the formation of the ice pavement bond. In theory continued application will ensure that no ice pavement bond is formed, keeping roads free of snow and ice during storms. Anti-icing is the application of solid or liquid chemical to the road surface prior to the precipitation event. Liquid chemical application has proven to work better and is therefore used more often. The chemicals are used to lower the freezing point of water so the snow does not bond to the pavement surface. There are five liquid chemicals that are used for anti-icing in the USA. These chemicals are NaCl , CaCl_2 , Calcium Magnesium Acetate ($[\text{CaMg}_2(\text{CH}_3\text{COO})_2]_6$), Potassium Acetate ($\text{KC}_2\text{H}_3\text{O}_2$), and Magnesium Chloride (MgCl_2) [US-FHWA 1996]. MgCl_2 is the most popular of the five. For anti-icing to work,

accurate weather information and pavement temperatures are a must. This is where thermal pavement modeling can help. With the development of RWIS stations, advanced weather forecasting models, and pavement/snow temperature forecasting models winter operations supervisors can more accurately choose where to send their anti-icing vehicles to fight storms more effectively.

Input Models

As mentioned in the introduction there are two models which will eventually provide the inputs for the model presented here. These two models are the Computational Albedo Routine (CAR) and the Radiation Thermal Road Temperature Model (RadThermRT) [Beddoe 2001, ThermoAnalytics 2000].

CAR.

CAR was directly adapted from the parameterization of albedo by Marshall [1989]. Albedo (α) is defined as the ratio of reflected (I_r) to incident (I) solar radiation, shown below [Gray and Male 1981]

$$\alpha = \frac{I_r}{I}. \quad (1)$$

Her computer program is called SNOALB. Marshall [1989] wrote the SNOALB program in Fortran utilizing the works of Marshall and Warren [1987], Rozenberg [1966], Wallace and Hobbs [1977] and Wiscombe and Warren [1980]. Professor R.L. Brown, Montana State University, converted the SNOALB code into C++ and later Beddoe [2001] used the converted SNOALB and created a user interface where inputs

are read from a text file and outputs are written to a text file. With the added interface and the conversion to C++, SNOALB was renamed CAR. The source code for the albedo user interface (main) program and the albedo routine are located in Appendix B. For details on the formulation of the albedo routine, see Chapter 2 of Beddoe [2001]. CAR calculates albedo of a uniform surface according to a known underlying surface albedo. The inputs for CAR are the same inputs as for SNOALB, which can be split into two categories atmospheric inputs and snow parameters. The atmospheric inputs are cosine of the solar zenith angle, atmospheric pressure, atmospheric transmittance for visible and near infrared radiation, diffuse fraction for visible and near infrared radiation, and the surface downflux for visible and near infrared radiation [Beddoe 2001]. The snow parameters are snow crystal grain radius, contaminate concentration, and the snow depth (g/cm^2). Snow depth accounts for the density of the snow. The grain size and impurity content have a strong influence on albedo. As grain size and impurity content increase, the albedo decreases [Beddoe 2001]. Beddoe [2001] (Chapter 3), indicates that the effects of zenith angle and diffuse radiation on albedo are minimal when compared to effects from grain size and impurity content. Based on Beddoe's [2001] findings, the model utilizes varying grain size and impurity content, from CAR.

RadThermRT.

RadThermRT was tailored from a computer model called PRISM (Physically Reasonable Infrared Signature Model) used by the U.S. Army to model surface temperatures of vehicles for use in infrared imagery [Adams and McDowell 1991]. The PRISM model was developed to predict infrared signatures of vehicles and considers

terrain as a background [Adams and McDowell 1991]. This same concept was expanded to terrain surrounding highways with the addition of digital elevation maps [Adams 1999]. Currently, the National Weather Service (NWS) ETA model, a global climate model, provides forecasted meteorological data in 40 km grid points. Advanced Regional Prediction System (ARPS) is a program that takes account for terrain, topography, and boundary conditions. At this time ARPS is being experimented with and is run twice, first scaling the meteorological data from 40 km grid points to 10 km, then again getting down to 1 km grid points [Personal communication with Adams]. After ARPS is run, weather forecast data is available at 1 km grid points, accounting for mountainous terrain. These weather predictions and US Geological Survey (USGS) 30-meter digital elevation maps (DEM) are the inputs for RadThermRT. RadThermRT then interpolates the 1 km grid points to match the 30 m resolution of the DEM. Using terrain features and the meteorological data, RadThermRT generates surface temperature forecasts. These surface temperatures take into account shadowing, conduction, convection, and radiation affects [Personal communication with Adams]. RadthermRT and ARPS provide all the necessary meteorological inputs for the model and in the future all three of the models will be interfaced. These interfaces will include transfer of wind speed (m/s), solar radiation (W/m^2), surface air temperature ($^{\circ}C$), relative humidity (%), barometric pressure (mbar), and cloud cover (%). Figure 3 is a flow chart representing how the models are linked together. The model presented here has been developed to eventually interface with RadthermRT.

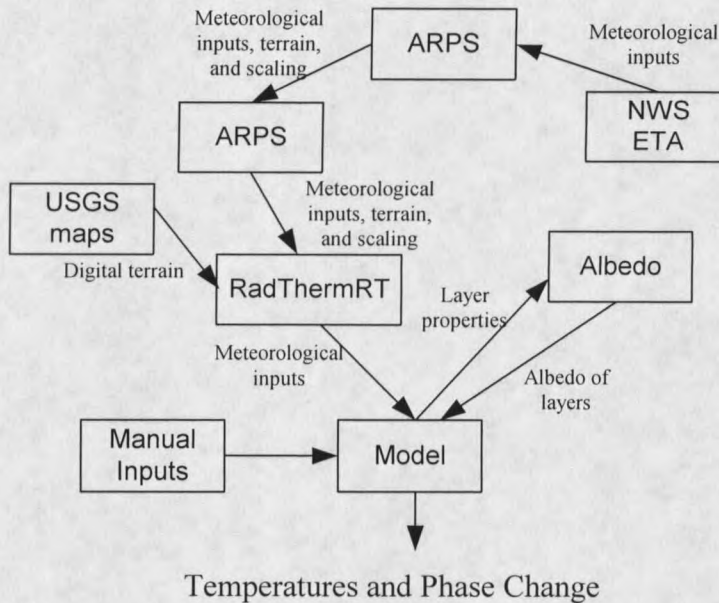


Figure 3. Flow chart of how the three models interact.

Previous Road/Ice Temperature Modeling

Numerous models have been developed for the purposes of road surface temperature prediction and radiation on suburban snowpacks [Ishikawa et al. 1999, Naruse et al. 1988, Sass 1992, Shao and Lister 1996, Todhunter et al. 1991]. These models utilize heat balance characteristics to predict temperatures or whether the net radiation is positive or negative, in turn causing surface heating or cooling. Todhunter et al. [1991] developed a heat balance model to predict net radiation over suburban snowpacks for the purpose of studying snow hydrology. Because snowmelt and rain on snow events differ from the hydrological models of rainfall, the model presented here was developed. Todhunter et al. [1991] uses a balance of solar radiation, long-wave radiation, substrate heat flux

(conduction), and turbulent flux of sensible heat (convection) to predict snowmelt. The snow is modeled as a continuous ripe snowpack. The term ripe snowpack indicates a snowpack that has uniform depth and has undergone complete metamorphism. Complete metamorphism is a process in which by melting and recrystallization, wind loading and settling, the physical properties of a snowpack have changed over time until it is able to release water during snowmelt periods [Todhunter et al. 1991]. Ishikawa et al. [1999] developed an energy balance model that includes six different heat fluxes (sensible heat, conductive heat, heat gained from rain, heat from vehicles, net radiation, and latent heat from evaporation). At 0°C , if the net heat flux is positive, then it is assumed that melting can occur, and vice versa, if the net flux is negative, freezing will occur. Ishikawa et al. [1999] studied in great detail how the heat flux from vehicles affects snowmelt. When vehicles are driving on the road, they shade the ground. If numerous vehicles drive bumper to bumper, the time that the road is covered by vehicles is considered shade time. While the road is covered, the vehicles emit infrared radiation. If the infrared radiation exceeds the total heat loss, the possibility for road heating or snowmelt can occur [Ishikawa et al. 1999]. The total heat loss takes into account the reduced short-wave radiation. Ishikawa et al. [1999] showed that a shade time of 20 minutes per hour resulted in an increase in the long-wave radiation by 50% and this resulted in a positive heat balance on the road. A shade time of 20 minutes per hour is comparable to a busy urban street, since the model is focusing on rural highways vehicle heat fluxes are not considered to be important.

Shao and Lister [1996] have a model that uses an unsteady one-dimensional heat conduction equation (similar to this model) to forecast road conditions up to 3 hours in advance. Their model uses conduction, solar radiation, long-wave radiation, sensible and latent heat fluxes to predict the road surface state, such as dry, wet, frost, or ice. This is done with the consideration of a previous temperature and the current precipitation status, and the exchange of moisture between the road surface and the overlying atmosphere [Shao and Lister 1996]. The surface state estimates are highly dependent on the predicted road temperature. If the road temperature is below 0° C and the road surface has been or is soon to be wet, ice will form. Naruse et al. [1988] considered both mechanical and thermal effects of vehicles passing on roads. They used an energy balance with solar radiation, surface albedo, net long-wave radiation, sensible heat, conductive heat, and the latent heat for melting along with a mass balance of a snow column on the road surface. Naruse et al. [1988] neglected the possibility that the column could melt from the bottom and the small amounts of evaporation at the surface. Since short-wave radiation can penetrate snow, depending on the thickness, and warm the pavement surface, present model includes melt from the bottom for this application. Sass [1992] balances heat transfer to predict road temperatures. In addition to using heat transfer concepts, Sass [1992] also uses mass latent heat to predict melting or freezing, and fluid dynamics to predict if ice melt will run off. Of the four models reviewed, Sass's [1992] model for the prediction of road temperatures and ice is the most similar to the model to be presented.

There are two major differences between the model presented here and the models outlined above. The first difference is that the other models consider the ice as one layer, no matter what the thickness of the ice/snow. The model developed here separates the snowpack into 1 mm layers. The second difference is the model presented here takes into account the physical properties of the snow/ice (e.g. density, grain size, impurity content, specific heat, and thermal conductivity). Although Narsue et al. [1988] looked at bulk density, only one layer was considered, not multiple layers of varying density. Incorporating individual layers and using physical properties makes it possible to calculate where and when melt is going to occur. Impurities play a large role in how all the layers are going to absorb solar radiation. Where specifically in the snow/icepack melt is going to occur is very important to winter operations. For example, if a winter maintenance supervisor knew that the solar radiation would penetrate through the ice/snow and be absorbed at the pavement, causing melting at the pavement ice interface, there would be no need for chemical application to break the pavement ice bond. On the other hand, if the supervisor knew because a layer of dust is absorbing the solar radiation and melt is only occurring in the center of the snowpack the need for chemical application is a must to break the pavement ice bond. These ideas and more are the driving factors behind the derivation of the model and will be explored in the following chapter.

CHAPTER 3

METHODOLOGY

In this chapter the derivations, equations, physical dimensions, and problem solving techniques will be introduced, developed, and explained. Also included in chapter 3 is an explanation of the validation experiment. Integrated in the discussion of the validation experiment section will be the purpose and goals of the experiment, information on the equipment used, and methods used for constructing the experimental setup.

The Model

The model is written using a programming package called MATLAB. This package provides a very powerful mathematical solver as well a fully functional numerical code language [Higham and Higham 2000]. The source code for the model can be found in Appendix A.

A one-dimensional simplification is used for this model. The model simulates a typical cross-section of an asphalt highway and is split into two parts: the road sub-grade and the snow/ice. The road sub-grade is further broken down into three more sections: sand, unbound rock aggregate, and bituminous asphalt. For the model road sub-grade dimensions follow the design of a typical highway, the top bituminous asphalt is 10 cm thick, the unbound rock aggregate is 30 cm deep, and the sand fills the last 60 cm, totaling 1 meter into the ground [Huang 1993]. In the model, snow and ice have variable physical properties (e.g. density, specific heat, thermal conductivity, etc.) with respect to

time, but the properties for the road sub-grade are fixed. Table 2 lists the specific heat (J/kg-K), the density (kg/m^3), and the thermal conductivity (W/m K) for the road sub-grade [Tan et al. 1997, White 1991].

Table 2. Physical properties of the road sub-grade.

Road sub-grade \ Properties	density (kg/m^3)	specific heat (J/kg-K)	Thermal Conductivity (W/m-K)
bituminous asphalt	2203	1135	1.34
unbound rock aggregate	1528	1106	0.72
sand	1500	800	0.3

The node spacing was broken down as follows: from -100 cm to -35 cm the spacing was 5 cm (14 nodes), from -35 cm to -5 cm the spacing was 1 cm (30 nodes), from -5 cm to the pavement surface the spacing was 1 mm (50 nodes) totaling 94 nodes through the road sub-grade. The ice/snow on top of the pavement was spaced with 1 mm increments as well. With the goal of having 1 mm ice/snow layers an unequal node spacing was chosen to reduce the models running time (Figure 4). This gradual decrease in node size from the lower boundary condition to the asphalt surface was used to minimize the error when solving the model numerically.

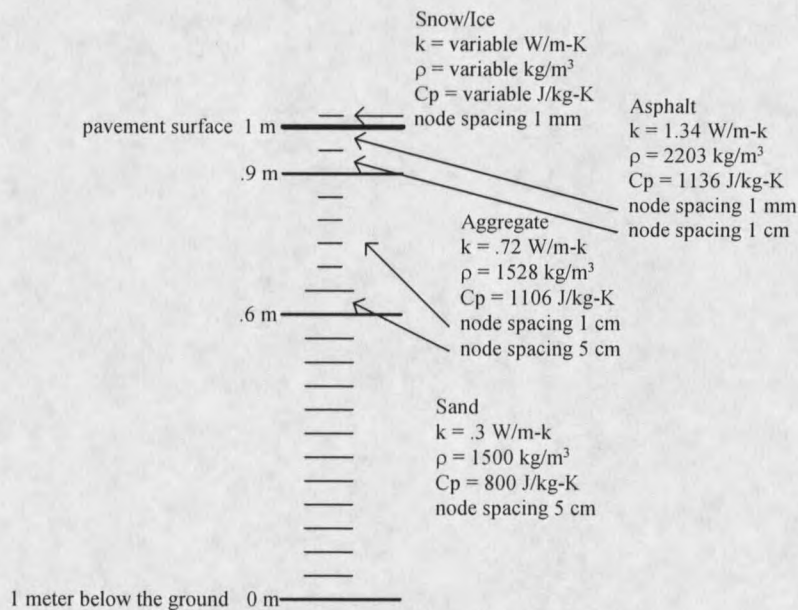


Figure 4. Geometry and node spacing for the model.

A 1 m deep boundary was chosen because at this depth the daily oscillation in temperature is negligible; this is defined as the diurnal depth. Figure 5a represents soil temperatures 2, 5, 8, 20, and 40 inches into the ground. The temperature profiles for this graph came from Fort Assiniboine, MT, site 2019, Montana Natural Resources Conservation Services (NRCS), United States Department of Agriculture (USDA). At 40 in (~1 m) the daily fluctuation is minimal therefore this depth was chosen for the lower boundary condition. Although the sub-grade material differs from Fort Assiniboine, to the area of interest, the data from Fort Assiniboine was the only available that was felt to be representative. The historical data at 40 in (~1 m) is well represented by a sinusoidal curve (Figure 5b). A sinusoidal function was fit to the data and is used as the temperature lower boundary condition,

$$T_g = 8.2 \cdot \sin \left[(D_{oyr} - 133) \cdot \frac{2 \cdot \pi}{365} \right] + 10.3, \quad (2)$$

where D_{oyr} is the day of the year (1-365) and T_g is the ground temperature ($^{\circ}\text{C}$) 1 m below the surface. The sinusoidal ground temperature function has a standard deviation of 1.235.

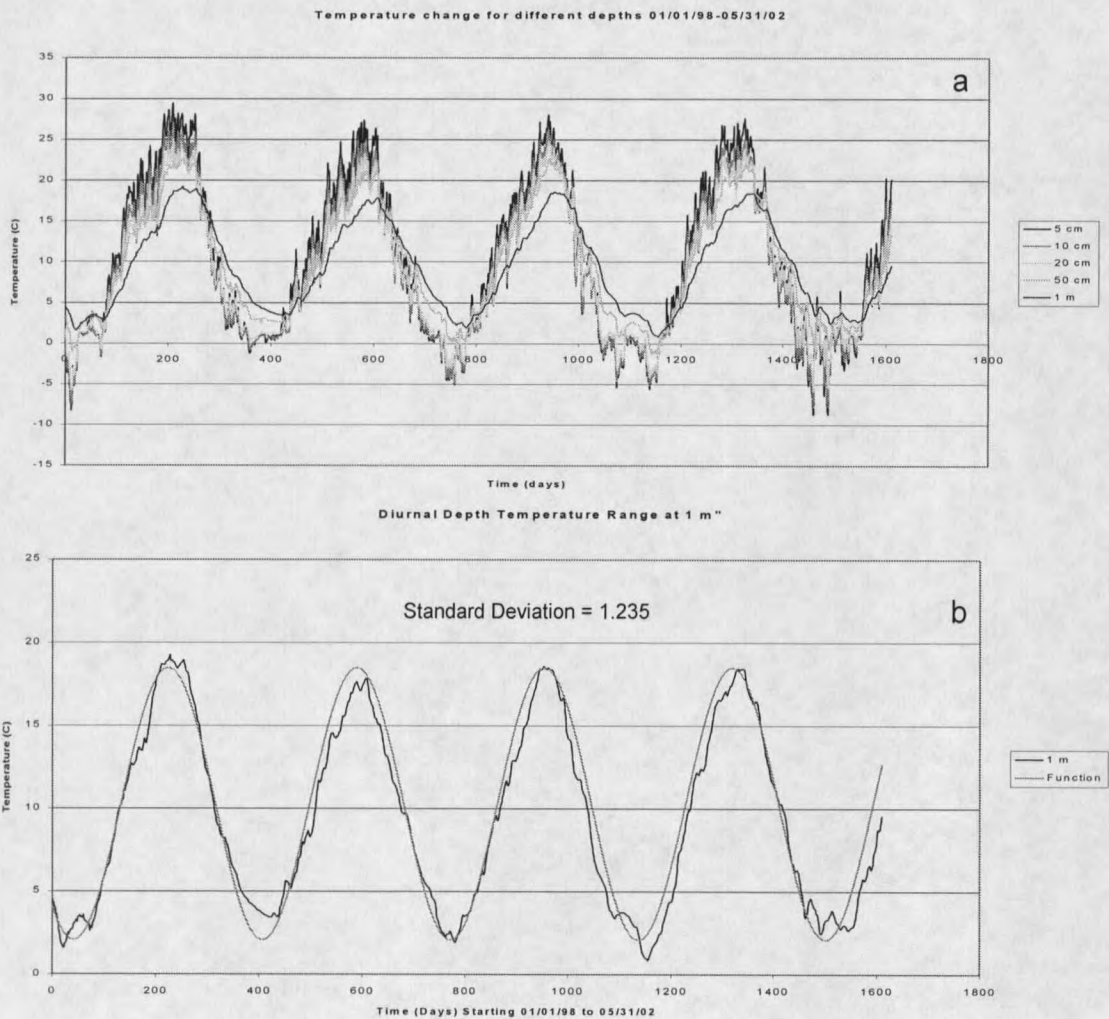


Figure 5. Temperature fluctuations vs. time at the Fort Assiniboine site. (a) presents all five of the soil depths (b) presents the 1 m depth with the sinusoidal curve.

Inputs from RadthermRT as stated earlier are solar radiation (W/m^2), air temperature ($^{\circ}\text{C}$), barometric pressure (mbar), relative humidity (%), wind speed (m/s), and cloud cover (%). Direct inputs into the model are temperature of the top layer of ice (T_{top} $^{\circ}\text{C}$), number of 1 mm layers above the pavement surface (n_l), density (ρ kg/m^3), grain size (mm), soot content (ppm), and if the layer is something other than snow or ice, specific heat (J/kg-K) and thermal conductivity (W/m K). If the layers are snow or ice, specific heat (C_p) and thermal conductivity (k) are calculated from equations by [Gray and Male 1981] and [Brandt and Warren 1993] respectively,

$$C_p = 2.115 + .00779 \cdot T_{top}, \quad (3)$$

$$k = 0.021 + 2.5 \cdot \rho^2. \quad (4)$$

Specific heat is calculated in (kJ/kg-C) then converted to (J/kg-K). Layer albedo is calculated using the CAR program. Density, grain size, underlying albedo, and soot content are passed into the CAR model and the layer albedo is passed back into the model. At this time the two programs are not specifically linked, so layer albedo is manually input into the model. The two models are written in different languages, MATLAB and C++. To create a communication process between MATLAB and C++ is laborious and complicated, therefore it was faster to input the albedos directly.

Steady State Heat Conduction.

Fourier's steady state heat conduction law is used to calculate the initial temperature profile for the model. Fourier's 1-D law of heat conduction [Bird et al. 2002, Black and Hartley 1996, Cengel and Boles 1994, Ozisik 1993] is given by,

$$q_y = -k \frac{\partial T}{\partial y}, \quad (5)$$

where q is a heat flux (W/m^2), k is the thermal conductivity ($\text{W}/\text{m}\cdot\text{K}$), and $\left(\frac{\partial T}{\partial Y}\right)$ is the temperature gradient ($^\circ\text{C}/\text{m}$). To calculate the steady state temperature profile, heat flux is used to calculate the temperature for every layer. Using boundary conditions the surface temperature, T_{top} , and the ground temperature at 1 m depth, T_g , the heat fluxes for each layer are set equal to each other and solved simultaneously. This provides the temperatures at each layer.

Long-wave Radiation.

Cooling or heating due to the emission of thermal infrared (long-wave) radiation to the atmosphere only occurs to upper few millimeters of a snowpack [Brandt and Warren 1993]. Snow or ice is essentially opaque to long-wave radiation ($400 - 1 \cdot 10^5$ nm), because a neighboring grain only absorbs radiation emitted by a neighboring grain. Therefore only the topmost grains can lose significant amounts of heat by radiation to the atmosphere [Brandt and Warren 1993]. For this reason, the model distributes the long-wave radiation flux over the top two layers of ice/snow. The long-wave radiation flux (Q_{lw}) for the model is the difference between incoming (Q_{lw_in}) and outgoing (Q_{lw_out}) long-wave radiation [Ishikawa 1999, Shao and Lister 1996, Sass 1992, Pluss 1997]

$$Q_{lw} = Q_{lw_in} - Q_{lw_out}. \quad (6)$$

Most long-wave radiation reaching the surface of the earth is emitted from the lowest layers of the atmosphere, therefore incoming long-wave radiation can be estimated from

air temperature (T_{air} (K)), water vapor pressure (e_a (kPa)), and cloud cover (cc (%)) denoted by [Plus 1997],

$$Q_{lw_in} = \left[\left(0.23 + 0.483 \cdot \left(\frac{e_a}{T_{air}} \right)^{1/8} \right) \cdot (1 - cc^3) + 0.963 \cdot cc^3 \right] \sigma \cdot T_{air}^4, \quad (7)$$

where σ is the Stefan-Boltzman constant ($\sigma = 5.67 * 10^{-8} \text{ W/m}^2 \cdot \text{K}^4$). Outgoing long-wave radiation, Q_{lw_out} , of a snow surface is obtained by [Plus 1997],

$$Q_{lw_out} = \varepsilon_s \cdot \sigma \cdot T_s^4 + (1 - \varepsilon_s) \cdot Q_{lw_in}, \quad (8)$$

where ε_s is the emissivity of the snowpack surface and T_s is the top layer (node 94 + n_1) snow temperature (K). Emissivity, generally varying between 0 and 1, accounts for the emitting properties of the particular radiating surface. The emissivity of snow was found to range between values of 0.985 – 0.990 depending on viewing angle and grain size [Dozier and Warren 1982]. For the model, the average was used for the emissivity of snow (ε_s).

Saturation Vapor Pressures.

Vapor pressures for the surface (e_s) and the air (e_a) are calculated using the Clapeyron-Clausius equation. Clapeyron-Clausius is a simplified version of the Clapeyron equation and is derived using the Gibbs equation and the Maxwell relations. The Gibbs equation [Black and Hartley 1996], is defined as,

$$dh = T \cdot ds + \nu \cdot dP, \quad (9)$$

where dh is the change in enthalpy (kJ/kg), T is the temperature (K), ds is the change in entropy (kJ/kg-K), ν is the specific volume (m^3/kg), and dP is the change in pressure

(kPa). The Maxwell relation relates the partial derivative of the properties (pressure (P), specific volume (ν), temperature (T), and entropy (s)) of a simple compressible system. A system can be considered simple compressible system in the absence of electrical, magnetic, gravitational, motion, and surface tension effects [Cengel and Boles 1994]. The Maxwell relationship used is given by [Cengel and Boles 1994],

$$\left(\frac{\partial P}{\partial T}\right)_{\nu} = \left(\frac{\partial s}{\partial \nu}\right)_T, \quad (10)$$

where the subscripts ν and T are specific volume and temperature, respectively. During a phase change process, the pressure is the saturation pressure, and only depends on the temperature [Cengel and Boles 1994] and thus can be written as,

$$\left(\frac{\partial P}{\partial T}\right)_{sat} = \frac{s_{fg}}{\nu_{fg}}. \quad (11)$$

Combining the Gibbs Equation (9) and the Maxwell relationship Equation (3), remembering that the pressure is constant (i.e. $dP = 0$), results in the Clayperon equation.

$$\left(\frac{\partial P}{\partial T}\right)_{sat} = \frac{h_{fg}}{T \cdot \nu_{fg}}, \quad (12)$$

where the subscripts g and f refer to the states of saturated vapor and saturated liquid, respectively, and h_{fg} is the enthalpy of vaporization. The enthalpy of vaporization is equal to the latent heat of phase change (L_e), and can be approximated by a single value for small temperature changes [Cengel and Boles 1994]. At low pressures $\nu_g \gg \nu_f$, and thus $\nu_{fg} \cong \nu_g$. Treating the vapor as an ideal gas [Black and Hartley 1996] gives,

$$\nu_g = \frac{R \cdot T}{P_g}, \quad (13)$$

where R is the gas constant for water vapor (0.462 kJ/kg-K) and P_g is the saturation vapor pressure (kPa). Substituting L_e for h_{fg} into the Clapeyron Equation (12) and combining that with the ideal gas law Equation (13) produces,

$$\left(\frac{dP}{P}\right)_{sat} = \frac{L_e}{R} \cdot \left(\frac{dT}{T^2}\right)_{sat} \quad (14)$$

Integrating Equation (14) with limits between (T, T_o) and (P_g, P_o) yields,

$$\ln\left(\frac{P_g}{P_o}\right) = \frac{L_e}{R} \cdot \left(\frac{1}{T_o} - \frac{1}{T}\right) \quad (15)$$

Rearranging terms presents the form of the Clapeyron-Clausius equation used in the model to calculate saturation vapor pressure of the surface (e_s) and the saturation vapor pressure of air (e_a).

$$P_g = P_o \cdot e^{\left(\frac{L_e}{R} \cdot \left(\frac{1}{T_o} - \frac{1}{T}\right)\right)}, \quad (16)$$

where P_o = reference saturation pressure ($P_o = 0.61173$ kPa),

T_o = reference saturation temperature ($T_o = 0.01$ C),

P_g = saturation vapor pressure (kPa) (e_s or e_a) at temperature T ,

T = temperature (K),

R = gas constant (kJ/kg-K).

Because air is not always saturated, relative humidity, RH, is taken as an input for the model. When using the Clapeyron-Clausius equation under conditions that are not saturated, relative humidity is used to calculate partial pressure of the water vapor. The equation is presented below [Hartley and Black 1996]

$$P_v = RH \cdot P_g, \quad (17)$$

where P_g is the saturation vapor pressure (kPa) and P_v is the partial pressure of the water vapor (kPa).

Turbulent Fluxes.

The latent heat flux due to evaporation and sublimation, Q_e (W/m^2) is only accounted for in the top layer of the ice/snow. The latent heat flux is driven by the vapor pressure gradient between air and the surface. The equation used in the model is represented below [Ishikawa et al. 1999],

$$Q_e = \frac{0.622 \cdot \rho_{air} \cdot L_e \cdot K_e \cdot V_w \cdot (e_a - e_s)}{P_{atm}}, \quad (18)$$

where L_e = latent heat of water vaporization (kJ/kg),

P_{atm} = atmospheric pressure (kPa),

V_w = wind speed (m/s),

e_a = water vapor pressure of air (kPa),

e_s = water vapor pressure of the surface (kPa),

K_e = dimensionless transfer coefficient for water vapor ($K_e = 0.0023$),

ρ_{air} = density of air (kg/m^3).

Sensible (convective) flux (Q_h W/m^2) is also only accounted for at the surface of the snow/ice air interface. The equation used for convection is given by [Ishikawa et al. 1999],

$$Q_h = \rho_{air} \cdot C_p \cdot K_h \cdot V_w \cdot (T_{air} - T_s), \quad (19)$$

where C_p = specific heat of air (J/kg-K),

K_h = dimensionless transfer coefficient for heat ($K_h = 0.0023$),

V_w = wind speed (m/s),

ρ_{air} = density of air (kg/m^3),

T_{air} = air temperature ($^{\circ}\text{C}$ or K),

T_s = temperature of the top snow/ice surface ($^{\circ}\text{C}$ or K).

Air density (ρ_{air}) is calculated by using the ideal gas law shown as,

$$\rho_{air} = \frac{P_{atm}}{R \cdot T_{air}}, \quad (20)$$

where P_{atm} = is the atmospheric pressure (kPa), R is the gas constant for air ($R = 0.287$ kJ/kg-K), and T_{air} is the temperature of the air (K) [Hudson and Nelson 1990].

Solar Radiation.

The penetration of visible radiation (400 – 750 nm) has little effect on the ground surface in deep snowpacks. However, in a shallow snowpack less than (20 - 30 cm) solar radiation can penetrate through the pack, warming the ground surface, providing energy for heating the snow, and in some cases snowmelt [Gray and Male 1981]. Because of the absorptive properties of snow, and even pure bubble free ice, solar radiation penetrating a snowpack is absorbed. Although the fraction absorbed and converted to heat is very small, it can accumulate, due to snow's poor heat conductivity [Yosida 1960]. The addition of highly absorptive impurities into a snowpack, can increase the amount and concentration of solar radiation absorbed by 50 – 200 times, depending on the impurity [Warren 1984]. Bouger's law is used to represent the amount of solar radiation transmitted through a layer (I) given by [Gray and Male 1981, Pluss 1997],

$$I = I_o \cdot e^{(-k \cdot dy)}. \quad (21)$$

By subtracting the amount of radiation transmitted through and reflected by the layer (I) from the initial amount of radiation (I_0), the amount of radiation absorbed in the layer (I_a) can be calculated.

$$I_a = I_0 - I_t \cdot e^{(-k \cdot dy)}, \quad (22)$$

where k is the extinction (absorption) coefficient (1/m) and dy is the thickness of the layer (m).

Grenfell and Perovich [1981] and Perovich and Govoni [1991] have studied radiation absorption coefficients for pure bubble free ice in great detail. Grenfell and Perovich [1981] provide extinction coefficients for pure bubble free ice for wavelengths ranging from 400 – 1400 nm. Table 3 displays the extinction coefficients of pure bubble free ice for the visible wavelengths (400 – 750 nm). The absorption coefficients in the visible range were totaled and averaged to provide a single value absorption coefficient that the model could use ($k_{ice} = 0.231$ 1/m).

Table 3. The extinction coefficients for pure bubble free ice in the visible range (400-700 nm), (reproduced from table 1 page 7449 Grenfell and Perovich 1981).

Absorption wavelength (nm)	coefficient k (1/m)	Absorption wavelength (nm)	coefficient k (1/m)	Absorption wavelength (nm)	coefficient k (1/m)	Absorption wavelength (nm)	coefficient k (1/m)
400	8.50E-02	500	4.79E-02	600	1.20E-01	700	5.20E-01
410	7.70E-02	510	5.26E-02	610	1.42E-01	710	6.09E-01
420	6.77E-02	520	5.45E-02	620	1.74E-01	720	7.03E-01
430	6.09E-02	530	6.03E-02	630	2.08E-01	730	7.41E-01
440	5.45E-02	540	6.83E-02	640	2.40E-01	740	8.35E-01
450	4.30E-02	550	7.10E-02	650	2.76E-01	750	9.84E-01
460	4.19E-02	560	7.38E-02	660	3.16E-01		
470	4.14E-02	570	7.75E-02	670	3.54E-01		
480	4.30E-02	580	8.76E-02	680	3.86E-01		
490	4.57E-02	590	1.04E-01	690	4.38E-01		

The magnitude of the extinction coefficient depends on factors such as density, wavelength, particle size, number of snow grains, extinction cross-section, and the imaginary part of the refractive index. Theories such as Rayleigh and Mie scattering are used to model the optical properties of snow [Aoki et al. 2000, Beddoe 2001, Wiscombe and Warren 1980a, 1980b]. Due to the complexity of incorporating such theories as Rayleigh and Mie scattering into a numerical model, the model presented here estimates the extinction properties of snow by using an effective depth of snow, ED , and the extinction coefficient of pure bubble free ice ($k_{ice} = 0.231$ 1/m). The effective depth of snow, ED , is an imaginary depth used only to calculate the amount of absorption occurring in that specific layer. A similar method was used in Wiscombe and Warren [1980a and 1980b] to calculate if a snow pack is infinitely thick or if radiation will penetrate to the underlying surface using a liquid-equivalent depth. The effective depth, ED , is calculated by the ratio of the snow density and pure bubble free ice density, then multiplied by the actual (physical) snow/ice layer thickness.

$$ED = dy_i \cdot \frac{\rho_{ice}}{\rho_{snow}}, \quad (23)$$

where ρ_{ice} is the density of ice ($\rho_{ice} = 917$ kg/m³), ρ_{snow} is the density of snow (kg/m³), and dy_i is the actual (physical) layer thickness ($dy_i = 0.001$ m). The idea to use an effective depth function came from the fact that an equal layer of snow will absorb more than an equal layer of ice [Wiscombe and Warren 1980]. So, if the model has fixed layers of 1 mm and the only absorption coefficient known is that of pure bubble free ice the extinction in snow can be estimated through a geometrical relationship.

Aoki et al. [2000] provide estimates of extinction coefficients for some common impurities found in snow (dust and soot), based on experimental data and calculations. Aoki et al. [2000] used a scanning electron microscope (SEM) to take photographs of snow impurities on Nuclepore filters. The Mie theory was used to calculate the single-scattering parameters of the impurity particles; the imaginary part of the refractive index was measured [Aoki et al. 2000]. Absorption coefficients can be calculated using the following relationship [Aoki et al. 2000, Wiscombe and Warren 1980a],

$$\beta_a(\lambda) = \frac{4 \cdot \pi \cdot m_{im}(\lambda)}{\lambda}, \quad (24)$$

where $\beta_a(\lambda)$ = the absorption coefficient for a wavelength (1/m),

$m_{im}(\lambda)$ = the imaginary part of the refractive index for a wavelength (m),

λ = wavelength of light (m).

Figure 6 is a graph from Aoki et al. [2000] that provides the imaginary part of the refractive index for numerous materials. The materials of interest for this paper (soot and dust) are boxed. In Figure 6, box 1 and box2 provide values of the imaginary part of the refractive index for the soot and dust, respectively, in the visible wavelengths. With the use of Equation (24) and the imaginary part of the refractive index absorption coefficients are calculated and averaged over the visible wavelengths (see Table 4).

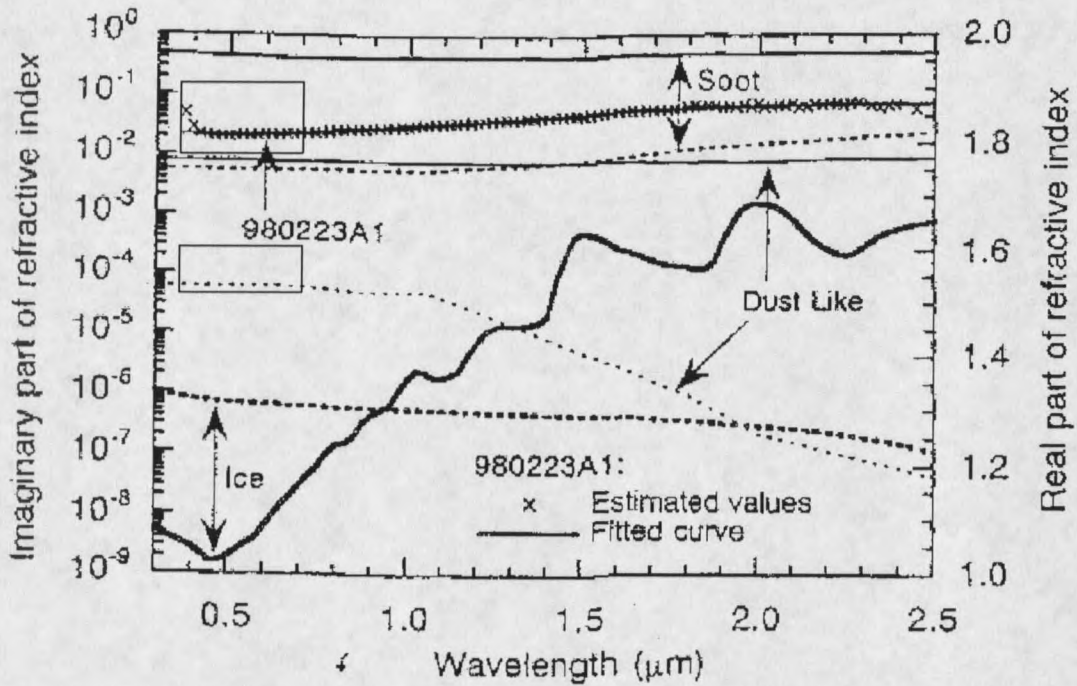


Figure 6. The imaginary part of the refractive index for soot and dust. (reproduced from Figure 8, page 10,227 Aoki 2000). [The square boxes represent the imaginary part of the refractive index for dust and soot in the visible wavelengths].

Table 4. Absorption coefficient calculations for both soot and dust using Equation (24).

Wavelength (m)	Imaginary part of refractive index (m)		Absorption coefficient (1/m)	
	dust	soot	dust	soot
4.00E-07	4.00E-05	9.00E-02	1.26E+03	2.83E+06
4.50E-07	4.00E-05	9.00E-02	1.12E+03	2.51E+06
5.00E-07	4.50E-05	9.00E-02	1.13E+03	2.26E+06
5.50E-07	4.50E-05	9.00E-02	1.03E+03	2.06E+06
6.00E-07	5.00E-05	8.50E-02	1.05E+03	1.78E+06
6.50E-07	5.00E-05	8.50E-02	9.67E+02	1.64E+06
7.00E-07	5.00E-05	8.00E-02	8.98E+02	1.44E+06
7.50E-07	5.00E-05	8.00E-02	8.38E+02	1.34E+06
Average absorption coefficient (1/m)			1.04E+03	1.98E+06

To account for impurities that are mixed in with the ice/snow, an averaging scheme needs to be introduced to effectively account for the absorption of both the ice and impurity together. An input into the model is impurity content in parts per million (ppm) this is used for averaging the absorption coefficient. The function is given by

$$k_{layer} = k_{ice} \cdot \left(1 - \frac{A_{imp}}{1 \cdot 10^6}\right) + k_{impurity} \cdot \left(\frac{A_{imp}}{1 \cdot 10^6}\right), \quad (25)$$

where k_{layer} is the average absorption coefficient (1/m), k_{ice} is the absorption coefficient of pure ice (1/m), $k_{impurity}$ is the absorption coefficient of the specified impurity, and A_{imp} is the amount of impurity in the layer (ppm) for the layer volume. Equation (25) is similar to an equation introduced in Wiscombe and Warren [1980a] used to calculate the real refractive index of a medium, where the medium is a volume-weighted average of the real refractive index of water and the suspended particles.

As light (solar radiation) travels into the snowpack, absorption is not the only important factor to consider, light scattering is also occurring. Depending on the albedo of the layers, either scattering or absorption can be the dominant factor controlling the absorption of solar radiation. If the material is high scattering, high albedo, solar radiation tends to be scattered out of the snowpack. If the material has a lower albedo, more solar radiation is absorbed or allowed to penetrate deeper into the snowpack. A numerical algorithm was created to account for scattering and absorption using Bouguer's law, (Equations 21 & 22), and the albedo relationship (Equation 1).

The numerical algorithm is explained first, followed by a graphical representation of the process (Figure 7). In Figure 7, the bold terms represent the solar fluxes being

absorbed. An initial beam of solar radiation, I_o , hits the top layer of snow/ice. Using Equation (1) radiation is reflected, I_r , or transmitted, I_t . Then Equation (21) is used to calculate how much radiation is available for the next layer; Equation (22) is used to calculate the amount of radiation absorbed in that layer. This process is repeated using the available radiation for the next deeper layer as the initial beam of radiation available to that layer until the radiation has penetrated to the pavement surface or not, depending on thickness, where all the radiation that has not been reflected is absorbed. In this paper, the underlying pavement surface represents bituminous asphalt, but this model can be used for to represent road surface such as concrete or others. The way to account for concrete would be to change the underlying surface layer parameters: density, specific heat, thermal conductivity, and albedo. Changing the albedo will dictate how much radiation is reflected at the road surface, in turn altering how much solar radiation will be absorbed at the road surface. The radiation that was reflected at each layer has now become the initial beam of radiation heading up into the snowpack, this process is repeated three times. All the radiations that have been absorbed in the layers are summed for the layer and used as the solar radiation heat fluxes (Q_{sw}).

of the differential equation solved in the model will resemble Fourier's law of transient heat conduction with energy generation terms [Bird et al. 2002, Lunardini 1988, Ozisik 1993, Shao and Lister 1996]. The First Law of Thermodynamics will be used to derive the differential equation used in the model [Black and Hartley 1996, Cengel and Boles 1994, Lunardini 1988] given as,

$$Q - W + (E_i - E_o) + Q_g = \Delta E_s, \quad (26)$$

where W is the mechanical work across the boundary, Q is the net heat transferred across the boundary, $(E_i - E_o)$ are the energies carried in and out of the system by mass flow, ΔE_s is the change in the sum of the potential, internal, and kinetic energy, and Q_g is the energy generated in the system and is split into two groups: heat source terms (Q_s), which include solar radiation, long-wave radiation, and turbulent fluxes, and the latent heat source term (Q_l). Each of the terms in the First Law will be expanded. In this model, mechanical work effects such as friction are neglected, therefore $W = 0$. Mass flow across the boundary is also going to be neglected (i.e., $E_i - E_o = 0$), indicating that percolation of either snow or rain will not be accounted for. Q the net heat transferred across the boundary is conduction. Figure 8 is a schematic drawing of one layer and will be used to assist in the derivation of heat conduction across the boundary.

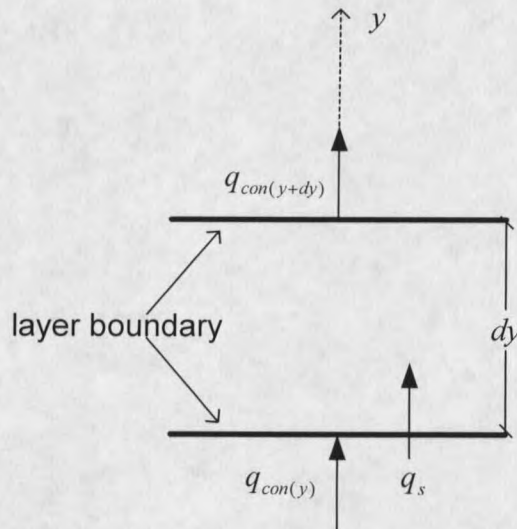


Figure 8. Schematic drawing of one layer used in the derivation of the transient heat conduction differential equation.

In one dimension the heat conduction coming into the layer ($q_{con(y)}$) is written using Fourier's law of conduction for the y -direction [Bird et al. 2002, Lunardini 1988],

$$q_{con(y)} = -k \cdot \frac{\partial T}{\partial y}. \quad (27)$$

Heat conduction leaving the boundary on the other side, $q_{con(y+dy)}$, is equal to the heat conduction coming in, $q_{con(y)}$, plus the change in energy through the layer multiplied by the layer thickness, dy , [Lunardini 1988] given as,

$$q_{con(y+dy)} = \left[-k \cdot \frac{\partial T}{\partial y} + \frac{\partial}{\partial y} \cdot \left(-k \cdot \frac{\partial T}{\partial y} \right) \cdot dy \right]. \quad (28)$$

The net conduction of energy in the y -direction over the area, A , and increment of time, dt , is written as,

$$Q_{con(y)} = \frac{\partial}{\partial y} \cdot \left(k \cdot \frac{\partial T}{\partial y} \right) \cdot dy \cdot A \cdot dt, \quad (29)$$

where k is the thermal conductivity of the layer (W/m-K). Energy transferred by turbulent fluxes and radiation fluxes will be considered as heat sources, q_s , per unit area and per unit time, and denoted as follows:

$$Q_s = q_s \cdot A \cdot dt, \quad (30)$$

where Q_l is the total flux over the area, A , and increment of time, dt . Q_l the latent heat source term in the system will be neglected for the moment in the derivation of the differential equation without phase change but will be used later in this chapter when phase change is being considered. The stored energy of the system is made up of macroscopic kinetic energy, potential energy, and internal energy [Black and Hartley 1996]. Changes in potential energy are assumed to be small and the system is not moving therefore changes in gravitational potential energy and kinetic energy are negligible. Reducing the change in stored energy, ΔE_s , to be only a function of internal energy, U (kJ/kg), [Lunardini 1988]

$$\Delta E_s = \frac{\partial}{\partial t} \cdot (\rho \cdot U) \cdot dy \cdot A \cdot dt. \quad (31)$$

When motion is not being considered internal energy can be written as the specific heat, C_p (J/kg-K), times the temperature, T (K), producing:

$$\Delta E_s = \rho \cdot C_p \cdot \frac{\partial T}{\partial t} \cdot dy \cdot A \cdot dt. \quad (32)$$

Recompiling the First law with Equations (29, 30, and 32), dividing out the area, A , and the time, dt , gives the differential equation solved in the model when phase change is not occurring,

$$\rho \cdot C_p \cdot \frac{\partial T}{\partial t} = k \cdot \frac{\partial^2 T}{\partial y^2} + \frac{qs}{dy} \quad (33)$$

To solve the differential Equation (33) numerically a variation of the Crank-Nicolson finite difference scheme is used. The Crank-Nicolson method is used to solve differential equations that are a first order differential equation equal to a second order differential equation similar to Equation (33), where the first order term, $\frac{\partial T}{\partial t}$, varies with respect to time and the second order term, $\frac{\partial^2 T}{\partial y^2}$, varies with respect to space. A Central differencing technique is used for the derivative approximations when using the Crank-Nicolson method. Below is a differential equation and the general form of the method to solve the differential equation.

$$\frac{\partial T}{\partial t} = \frac{\partial^2 T}{\partial y^2}, \quad (34)$$

$$\frac{T_i^{j+1} - T_i^j}{\Delta t} = \frac{1}{2} \left[\frac{T_{i+1}^j - 2 \cdot T_i^j + T_{i-1}^j}{(\Delta y)^2} + \frac{T_{i+1}^{j+1} - 2 \cdot T_i^{j+1} + T_{i-1}^{j+1}}{(\Delta y)^2} \right], \quad (35)$$

where the subscript i represents the spatial nodes and the superscript j represents time, $j+1$ describes a future time step. The Crank-Nicolson method is termed implicit for its ability to calculate new temperatures using both the present value of temperature at three spatial nodes and the predicted future values at three spatial nodes [Gerald and Wheatley

1994]. This method requires solving simultaneous equations at each time step usually requiring matrix inversion. The Crank-Nicolson method is often used because it is unconditionally stable for any time step, although it is more accurate with smaller time steps [Gerald and Wheatley 1994, Ozisik 1993]. Because the Crank-Nicolson method was created for equal sized spatial nodes, a variation of the method must be used to account for unequal mesh spacing. Figure 9 schematically displays the terms used in the second order unequal mesh central differencing scheme, where θ is the fraction of the standard spacing, dy [Gerald and Wheatley 1994].

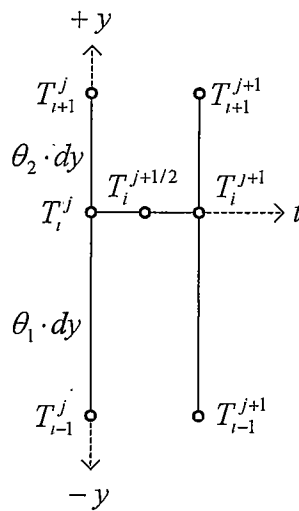


Figure 9. The unequal mesh used to find the solution technique to solve the second order differential equation.

The second order derivative is given by,

$$\frac{\partial^2 T}{\partial y^2} = \frac{\frac{(T_{i+1}^j - T_i^j)}{(\theta_2 \cdot dy)} - \frac{(T_i^j - T_{i-1}^j)}{(\theta_1 \cdot dy)}}{\frac{1}{2} \cdot (\theta_1 + \theta_2) \cdot dy} \quad (36)$$

Rearranging terms and making $\theta_1 = dy_1$ and $\theta_2 = dy_2$ gives

$$\frac{\partial^2 T}{\partial y^2} = 2 \cdot \left[\frac{dy_1 \cdot (T_{i+1}^j - T_i^j) + dy_2 \cdot (T_{i-1}^j - T_i^j)}{dy_1 \cdot dy_2 \cdot (dy_1 + dy_2)} \right], \quad (37)$$

where dx_1 and dx_2 are the distances between a node and the lower and upper nodes, respectively. The differential equation without phase change, Equation (33), is now broken into parts to show how each part is solved numerically. The first order term is solved using central differencing on the time step $t_{i+1/2}$ denoted by,

$$\frac{\partial T}{\partial y} = \frac{T_i^{j+1} - T_i^j}{\Delta t}. \quad (38)$$

Using the central differencing for the unequal mesh, as the average of the present and future time steps, the second order term of Equation (33) looks as follows:

$$\frac{k}{C_p \cdot \rho} \cdot \frac{\partial^2 T}{\partial y^2} = \frac{k}{C_p \cdot \rho} \cdot \left[\frac{dy_1 \cdot (T_{i+1}^j - T_i^j) + dy_2 \cdot (T_{i-1}^j - T_i^j)}{dy_1 \cdot dy_2 \cdot (dy_1 + dy_2)} + \frac{dy_1 \cdot (T_{i+1}^{j+1} - T_i^{j+1}) + dy_2 \cdot (T_{i-1}^{j+1} - T_i^{j+1})}{dy_1 \cdot dy_2 \cdot (dy_1 + dy_2)} \right]. \quad (39)$$

Substituting Equation (38) and Equation (39) into Equation (33) and rearranging yields the following finite difference approximation:

$$\frac{T_i^{j+1} - T_i^j}{\Delta t} = \frac{k}{C_p \cdot \rho} \cdot \left[\frac{dy_1 \cdot (T_{i+1}^j - T_i^j) + dy_2 \cdot (T_{i-1}^j - T_i^j)}{dy_1 \cdot dy_2 \cdot (dy_1 + dy_2)} + \frac{dy_1 \cdot (T_{i+1}^{j+1} - T_i^{j+1}) + dy_2 \cdot (T_{i-1}^{j+1} - T_i^{j+1})}{dy_1 \cdot dy_2 \cdot (dy_1 + dy_2)} \right] + \frac{q_m}{C_p \cdot \rho \cdot dy}. \quad (40)$$

Expanding and rearranging terms so all the unknown temperatures (future time steps) are on the left side gives the final numerical version of the differential equation:

$$\begin{aligned}
& -dy_2 \cdot T_{i-1}^{j+1} + \left[\frac{\rho \cdot C_p \cdot dy_1 \cdot dy_2 \cdot (dy_1 + dy_2) - k \cdot \Delta t \cdot (dy_1 + dy_2)}{k \cdot \Delta t} \right] \cdot T_i^{j+1} - dy_1 \cdot T_{i+1}^{j+1} = \\
& -dy_2 \cdot T_{i-1}^j + \left[\frac{\rho \cdot C_p \cdot dy_1 \cdot dy_2 \cdot (dy_1 + dy_2) - k \cdot \Delta t \cdot (dy_1 + dy_2)}{k \cdot \Delta t} \right] \cdot T_i^j - dy_1 \cdot T_{i+1}^j + \frac{2 \cdot dy_1 \cdot dy_2 \cdot q_{in}}{k}.
\end{aligned} \tag{41}$$

When solving the differential Equation (41) two boundary conditions (top and bottom) need to be imposed. The bottom boundary condition is the diurnal depth temperature, T_g , expressed by Equation (2). The top snow/ice surface is a node of interest and because the node is always changing temperature from the effects of long-wave radiation, turbulent, and radiation fluxes the top node cannot be set as a constant boundary condition. The most accurate approach is to write the energy balance at the surface node in terms of a finite difference approximation. Unfortunately, because this balance includes the surface temperature to the fourth power, the resulting relationship becomes nonlinear. To linearize this process, it is possible to introduce a gradient boundary condition. A phantom node is created above the actual surface and the temperature of the phantom node is used as the boundary condition, the phantom node temperature is presented based on an estimate of heat flux at the surface from the previous time step. This was done by using the steady state conduction, Equation (5) [Ozisik 1993]

$$k \cdot \frac{T_{phantom}^{j+1} - T_{i-1}^{j+1}}{2 \cdot \Delta y} = q_{jn}, \tag{42}$$

rearranging terms the phantom node boundary condition used in the model is shown as,

$$T_{phantom}^{j+1} = T_{i-1}^{j+1} - \frac{2 \cdot \Delta y \cdot q_{jn}}{k_n}, \quad (43)$$

where Δy is the ice/snow layer thickness ($\Delta y = 1$ mm), q_{jn} are the heat sources for the current layer in time, j , and the top layer, n , and k_n is the thermal conductivity of the top layer n (W/m-K).

Phase Change

As mentioned in chapter 2, the phase change of interest is for water going from a solid (snow/ice) to a liquid or liquid to solid. During phase change, energy is either absorbed or released as the ice thaws or freezes, respectively. The energy equation can be used to model phase change at an interface between liquid and solid given by [Lunardini 1988],

$$(q_1 - q_2) \cdot \Delta t \cdot A + q_s \cdot \Delta t \cdot A - W = \Delta E, \quad (44)$$

where $(q_1 - q_2)$ are respectively the conduction terms at the top and bottom of the phase change layer interface (W/m^2), W is the mechanical work term and will be considered to be zero, q_s is the sum of the heat source terms associated with radiation and turbulent fluxes (W/m^2), and ΔE is the change in energy due to phase change (W/m^2). The change in energy due to phase change can be written as follows: [Lunardini 1988]

$$\Delta E = m \cdot (h_s - h_l), \quad (45)$$

where m is equal to mass (kg), h_s refers to the enthalpy of the solid water (ice), and h_l is the enthalpy of liquid water. The change in enthalpy from solid to the liquid phase, $h_s - h_l$, is considered to be the latent heat of fusion, $L_f = 334$ kJ/kg. Dividing Equation (44) by

the area, A , and time differential, Δt , the right of Equation (44) can be expressed as follows:

$$\frac{\Delta E}{A \cdot \Delta t} = \rho \cdot L_f \cdot \frac{ds}{dt}, \quad (46)$$

where density of the layer changing phase is ρ (kg/m^3) and $\frac{ds}{dt}$ is the amount of the layer that has changed phase in time (m/s), Figure 10 is a drawing of a few layers and the hatched area represents Δs . Setting the conduction difference, $q_1 - q_2$, and the sum of the heat sources associated with the turbulent and radiation fluxes, q_s , equal to the change in energy due to phase change, ΔE , gives the phase change equation [Lunardini 1988]

$$\rho \cdot L_f \cdot \frac{ds}{dt} = -k_1 \cdot \frac{\partial T}{\partial y} + k_2 \cdot \frac{\partial T}{\partial y} + q_s, \quad (47)$$

where k_1 and k_2 are the thermal conductivities of the layer water and ice above and below the phase change interface.

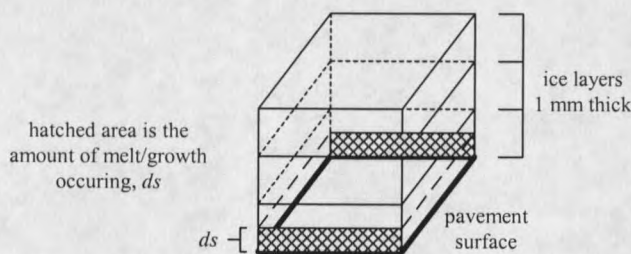


Figure 10. Graphical representation of where the ds was located in a melting layer.

The latent heat of fusion is actually associated with changes in internal energy of the material, but its effect is often accounted for as an energy generation term [Lunardini

1988]. The energy generation term, Q_l , neglected in the derivation of the differential equation without phase change can be written as follows: [Lunardini 1988]

$$Q_l = -q_l \cdot A \cdot dt, \quad (48)$$

and q_l is the energy generated or released during the change per unit area and time,

$$q_l = -\rho \cdot L_f \cdot \left(\frac{ds}{dt} \right). \quad (49)$$

To create the final differential equation with phase change used in the model, Equations (29, 30, and 48) are added and set equal to the energy stored in the system, ΔE_s , Equation (32)

$$-\rho \cdot L_f \cdot \frac{ds}{dt} \cdot A \cdot dt + q_s \cdot A \cdot dt + k \cdot \frac{d^2 T}{dy^2} \cdot dy \cdot A \cdot dt = \rho \cdot C_p \cdot \frac{dT}{dt} \cdot dy \cdot A \cdot dt. \quad (50)$$

Rearranging terms and dividing out the area, A , and the time, dt , yields the following differential equation, which was used in the model,

$$\rho \cdot L_f \cdot \frac{ds}{dt} + \rho \cdot C_p \cdot \frac{dT}{dt} \cdot dy = k \cdot \frac{d^2 T}{dy^2} \cdot dy + q_s. \quad (51)$$

When phase change occurs in this model, it will be handled one layer at a time. Because of this, phase change and temperature change need to be accounted for during every time step of the numerical solution. The temperature of the layer changing phase from solid to liquid or vice versa is fixed at 0° C. A layer will not begin to changing phase until the temperature has reached 0° C, at that point the energy from conduction and heat source terms for that layer will go into changing phase, not the layer's temperature. Not until all the water has refrozen or runoff will the layer again be able to change temperature. After temperatures are determined at each time step via the central

differencing approximation to the global energy balance, a first order central differencing scheme is used to solve Equation (47) for the phase change requirement. Rearranging terms to solve for Δs , the numerical approximation for Equation (47) is shown below,

$$\Delta s = \frac{\Delta t}{\rho \cdot L_f} \cdot \left[k_i \cdot \left(\frac{T_{i+1}^j - T_{i-1}^j}{2 \cdot \Delta y} \right) + q_i \right], \quad (52)$$

where the subscript i represents the layer that is changing phase.

Runoff

After a layer has melted all the way through (e.g. $ds = 0.001$ m) runoff is allowed to occur. Runoff time, t_{runoff} , was taken as the time that it takes for the farthest water, $d_{runoff} = 1$ m, divided by the average velocity, U_{avg} , of the flow given by

$$t_{runoff} = \frac{d_{runoff}}{U_{avg}}. \quad (53)$$

A layer will not be free of water until the runoff time has been reached. Due to the inability and complications to construct an experiment to measure t_{runoff} and inadequate documentation in the literature, basic flow mechanics models were used to estimate t_{runoff} . Numerous assumptions were made when solving both the Navies-Stokes equations and the shell momentum balance equation. Assumptions include: the column of snow does not collapse during runoff, incompressible flow, steady state, confined/unconfined flow, 1-D flow in the x-direction, velocities are only a function of the y-direction, pressure in all directions is neglected, and conservation of mass. The results of t_{runoff} were used to provide a result with an order of magnitude of accuracy. The t_{runoff} found in this section proved to be negligible compared to the times associated with the experiments.

Although, the times of runoff was considered negligible, for this study, the calculated times, t_{runoff} , were left in the model. They were left in the model for future applications where time of run could be an important factor.

Flow velocity was calculated using the Navier-Stokes equations described below. Highways are built on a slope for the purpose of water runoff, so the coordinate system will have the x-axis in the plane of the road perpendicular to the centerline, the z-direction will be normal to the x-axis in the plane of the road, and the y-direction was normal to the road surface perpendicular to the, x-axis and the z-axis. Flow was assumed to runoff from the centerline to the side of the road in the x-direction, therefore one-dimensional flow can be assumed. The x-component of the Navier-Stokes incompressible flow equation is denoted by [Bird et al. 2002, Street et al. 1996],

$$\rho \cdot B_x - \frac{\partial P}{\partial x} + \mu \cdot \nabla^2 u = \rho \cdot a_x, \quad (54)$$

where ρ is the density of water ($\rho = 1000 \text{ kg/m}^3$), B_x is the body force due to gravity in the x-direction ($B_x = -g \sin(\theta)$), θ is the road angle measured relative to horizontal, a_x is the acceleration in the x-direction (m/s^2), u is the velocity in the x-direction (m/s), μ is the viscosity of water ($\mu = 0.001781 \text{ N}\cdot\text{s/m}^2$), P is the pressure (kPa), and ∇^2 is the Laplacian operator. When expanding the Navier-Stokes equation, in the x-direction for spatial coordinates it is denoted by,

$$-\frac{\partial P}{\partial x} + \mu \cdot \left[\frac{\partial^2 u}{\partial x^2} + \frac{\partial^2 u}{\partial y^2} + \frac{\partial^2 u}{\partial z^2} \right] - \rho \cdot g \cdot \sin(\theta) = \rho \cdot \left(\frac{\partial u}{\partial t} + u \cdot \frac{\partial u}{\partial x} + v \cdot \frac{\partial u}{\partial y} + w \cdot \frac{\partial u}{\partial z} \right). \quad (55)$$

Conservation of mass, steady state, and 1-D flow was assumed to help reduce the Navier-Stokes equation. 1-D flow states that the velocity in the y-direction is equal to zero ($v(x,y,z) = 0$) and the velocity in the z-direction is equal to zero ($w(x,y,z) = 0$). With the use of 1-D flow and the continuity equation (i.e., mass conservation) for a constant density shown as [Bird et al. 2002, Street et al. 1996],

$$\frac{\partial u}{\partial x} + \frac{\partial v}{\partial y} + \frac{\partial w}{\partial z} = 0. \quad (56)$$

Flow in the x-direction is a function of only y, $u(y)$. Because the pressure in the x-direction is the same at both ends, the change in pressure in the x-direction was equal to zero and therefore can be neglected. Removing the pressure term, the neglected velocities, and from steady state the time rate term, $\frac{\partial u}{\partial t}$, reduces the Navier-Stokes equation to:

$$\mu \cdot \frac{\partial^2 u}{\partial y^2} = \rho \cdot g \cdot \sin(\theta). \quad (57)$$

When the water is running off between two layers, confined flow is assumed, therefore the boundary velocities are 0 m/s. Equation (57) can be integrated twice to find the velocity profile of the confined flow, U_c , shown below

$$\frac{\partial^2 u}{\partial y^2} = \frac{\rho \cdot g \cdot \sin(\theta)}{\mu}, \quad (58)$$

$$\frac{\partial u}{\partial y} = \frac{\rho \cdot g \cdot \sin(\theta)}{\mu} \cdot y + C_1, \quad (59)$$

$$U_c = \frac{\rho \cdot g \cdot \sin(\theta)}{2 \cdot \mu} \cdot y^2 + C_1 \cdot y + C_2, \quad (60)$$

Applying the boundary conditions at $y = 0$, $U_c = 0$, and at $y = Y$, $U_c = 0$ and solving for the integration constants provides the velocity profile for confined flow,

$$C_2 = 0; \quad C_1 = \frac{-\rho \cdot g \cdot \sin(\theta) \cdot Y}{2 \cdot \mu}, \quad (61)$$

$$U_c = \frac{\rho \cdot g \cdot \sin(\theta) \cdot y}{2 \cdot \mu} \cdot [y - Y] \quad (62)$$

where $\rho =$ is the density of water ($\rho = 1000 \text{ kg/m}^3$),

$g =$ is the gravitational force ($g = 9.81 \text{ m/s}^2$),

$\mu =$ is the viscosity of water ($\mu = 0.001781 \text{ Ns/m}^2$),

$\theta =$ is the road angle,

$Y =$ is the thickness of the layer ($Y = 1 \text{ mm}$),

$y =$ is the distance from 0-1mm where the velocity is of interest.

Equation (62) was used to get velocities in the x-direction every tenth of a millimeter in the y-direction, and for typical road angles 2° and 3° (road angles of 2° and 3° were chosen to account for the centerline to the side of the road slope variability [Huang 1993]). These velocities were added then divided by the number of increments to give an average velocity for each road angle. Next, the runoff times of 69.36 s and 46.25 s were calculated from the road angles 2° and 3° respectively (Figure 11a&b). Finally, these times were averaged to come up with a runoff time of 58 s for the model.

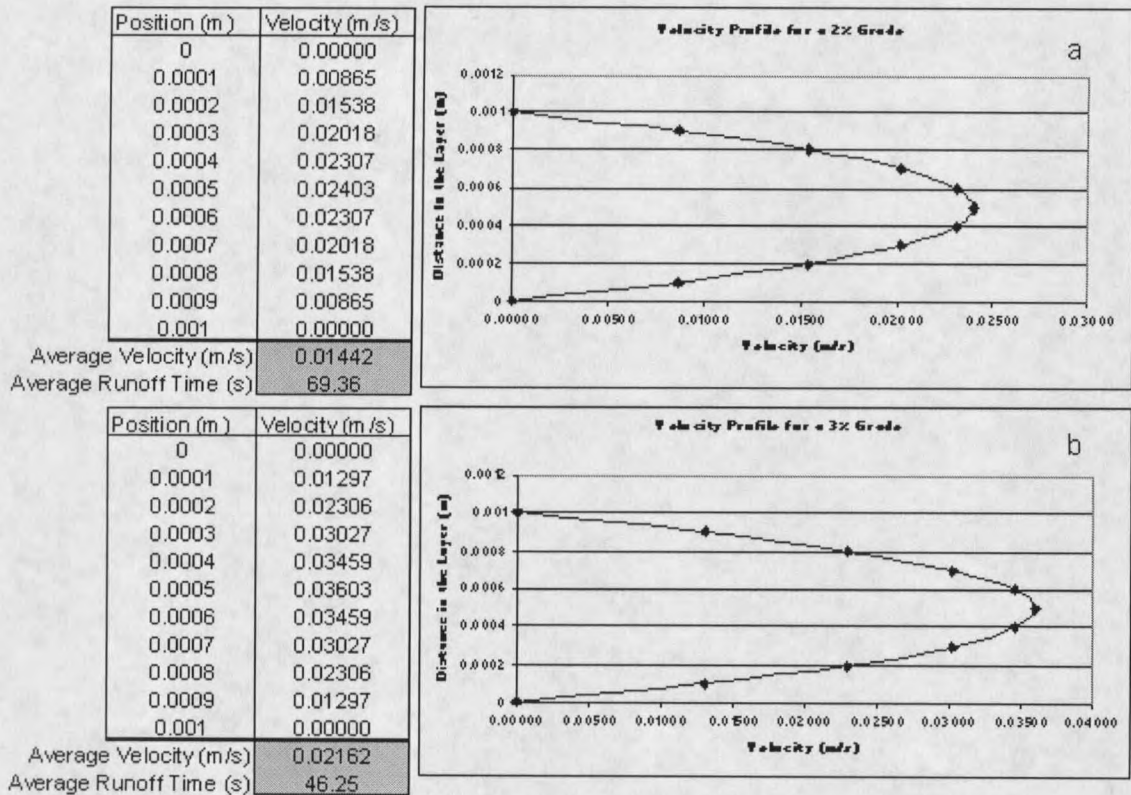


Figure 11. Velocity profiles calculated using the Navier-Stokes equation for confined flow and the calculation for the average runoff time. (a) for a 2% road grade (b) for a 3% road grade.

If runoff occurs at the top layer of snow or ice, confined flow was not a valid assumption. For this reason, the top layer was modeled as a falling film flow. To calculate the falling film flow velocity profile, U_f , a shell momentum balance was approximated [Bird et al. 2002]. The balance of momentum in the x-direction was of interest. For the same reasons as stated above flow will only occur in the x-direction with respect to y , $u(y)$. The first step of the shell balance was to define the shell, which was the thickness of the flowing water, y -direction, and the length the water flows in the x -

direction (Figure 12a). Using the shell, an equation can be written to resemble the in and out going momentums, Φ is the rate of momentum transport (Figure 12b),

$$L \cdot (\Phi_{xy}|_y - \Phi_{xy}|_{y+\Delta y}) + \Delta y \cdot (\Phi_{xx}|_{x=0} - \Phi_{xx}|_{x=L}) + L \cdot \Delta y \cdot B_y = 0. \quad (63)$$

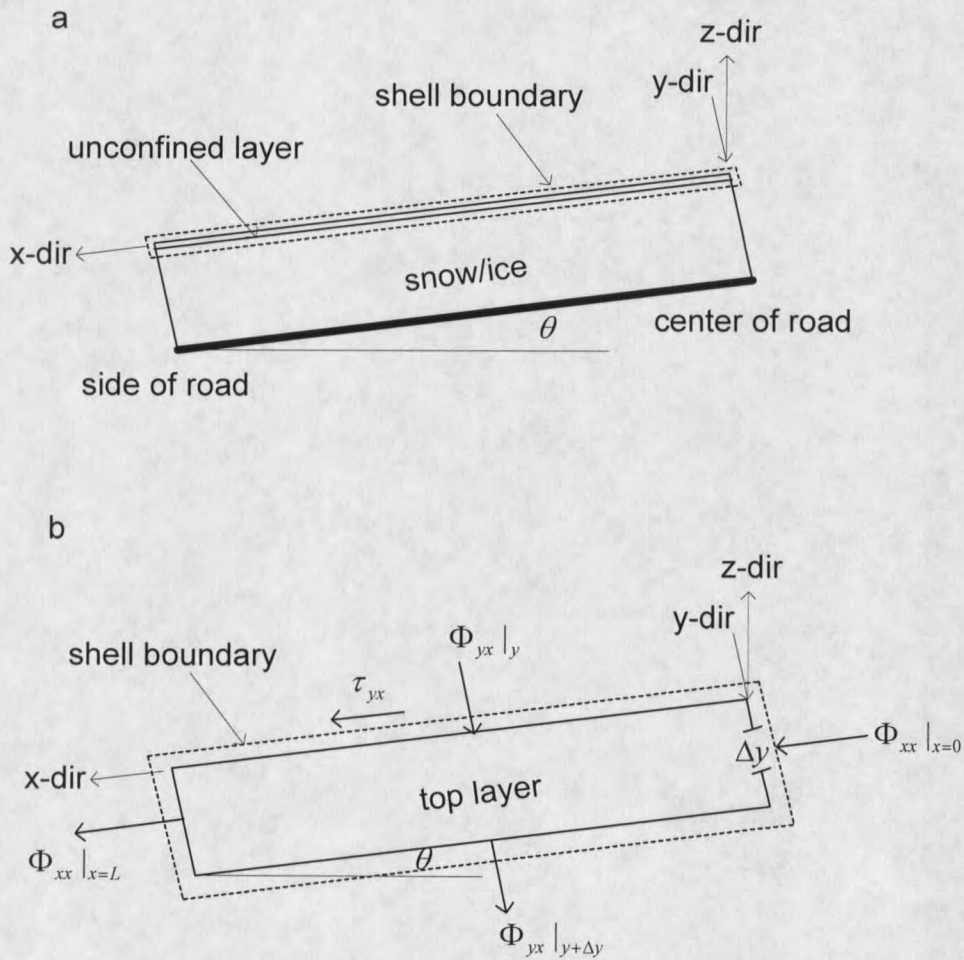


Figure 12. Drawing used for the flow of a falling film velocity. (a) shows where the unconfined layer is. (b) a blow up of the top layer and the shell boundary.

Rearranging the body force, B_y , to the other side of Equation (63) and replacing it with $\rho \sin(\theta)$, dividing through by $L \cdot \Delta y$, and taking the limit of Equation (63) as Δy approaches zero produces [Bird et al. 2002],

$$\frac{d\Phi_{yx}}{dy} - \frac{\Phi_{xx}|_{x=0} - \Phi_{xx}|_{x=L}}{L} = \rho \cdot g \cdot \sin(\theta), \quad (64)$$

where,

$$\Phi_{yx} = P + \tau_{yx} + \rho \cdot u_y \cdot u_x, \quad (65)$$

$$\Phi_{xx} = P + \tau_{xx} + \rho \cdot u_x \cdot u_x. \quad (66)$$

Φ_{xx} is the rate of momentum transfer on the x-face in the x-direction, Φ_{yx} is the rate of momentum transfer on the y-face in the x-direction (Figure 12b), from above $u(x) = 0$, thus reducing Equation (64) to,

$$\frac{d\tau_{yx}}{dy} = \rho \cdot g \cdot \sin(\theta), \quad (67)$$

where τ_{yx} is the momentum flux on the y-face in the x-direction (Figure 12b). Integrating Equation (67) and applying the boundary condition at $y = 0$, the momentum flux, $\tau_{yx} = 0$, because the momentum flux at a liquid gas interface was taken to be zero [Bird et al. 2002],

$$\tau_{yx} = (\rho \cdot g \cdot \sin(\theta)) \cdot y + C_1, \quad (68)$$

$$y=0; \quad \tau_{yx}=0 \rightarrow C_1=0, \quad (69)$$

$$\tau_{yx} = (\rho \cdot g \cdot \sin(\theta)) \cdot y. \quad (70)$$

Next, Newton's law of viscosity [Bird et al. 2002],

$$\tau_{yx} = -\mu \cdot \frac{du(y)}{dy}, \quad (71)$$

was substituted into the left side of Equation (70) producing,

$$-\mu \cdot \frac{du(y)}{dy} = (\rho \cdot g \cdot \sin(\theta)) \cdot y. \quad (72)$$

Equation (72) was then integrated and using $u(y) = 0$ as the other boundary condition at $y = \Delta y$, gives the falling film velocity, U_f ,

$$U_f = -\left(\frac{\rho \cdot g \cdot \sin(\theta)}{2 \cdot \mu}\right) \cdot y^2 + C_2, \quad (73)$$

$$y=0; \quad u(y)=0 \rightarrow C_2 = \left(\frac{\rho \cdot g \cdot \sin(\theta)}{2 \cdot \mu}\right) \cdot \Delta y^2, \quad (74)$$

$$U_f = \frac{\rho \cdot g \cdot \sin(\theta) \cdot \Delta y^2}{2 \cdot \mu} \cdot \left[1 - \left(\frac{y}{\Delta y}\right)^2\right], \quad (75)$$

where $\rho =$ is the density of water ($\rho = 1000 \text{ kg/m}^3$),

$g =$ is the gravitational force ($g = 9.81 \text{ m/s}^2$),

$\mu =$ is the viscosity of water ($\mu = 0.001781 \text{ Ns/m}^2$),

$\theta =$ is the road angle,

$\Delta y =$ is the thickness of the layer ($\Delta y = 1 \text{ mm}$),

$y =$ is the distance from 0-1 mm where the velocity is of interest.

To find the average velocity analytically of a falling film Bird et. al. [2001] gives,

$$U_{f,avg} = \frac{\int_0^{\Delta y} \int_0^{\Delta y} U_f \, dy \, dz}{\int_0^{\Delta y} \int_0^{\Delta y} dy \, dz} = \frac{1}{\Delta y} \cdot \int_0^{\Delta y} U_f \, dy, \quad (76)$$

$$U_{f,avg} = \frac{\rho \cdot g \cdot \sin(\theta) \cdot \Delta y^2}{2 \cdot \mu} \cdot \int_0^{\Delta y} \left[1 - \left(\frac{y}{\Delta y} \right)^2 \right] d \left(\frac{y}{\Delta y} \right), \quad (77)$$

$$U_{f,avg} = \frac{\rho \cdot g \cdot \sin(\theta) \cdot \Delta y^2}{3 \cdot \mu}. \quad (78)$$

Using the two road angles 2° and 3° , average velocities were calculated with Equation (78). Average velocities were used with Equation (53) to calculate the runoff times of 15.6 s and 6.94 s for road angles of 2° and 3° , respectively. These times were averaged to give a top layer runoff time of 11.28 s.

Runoff starts to be accounted for after a specific layer of snow or ice has melted (i.e., $ds = 1$ mm). Depending on where the layer that has melted, is either confined flow or unconfined flow will be chosen as which method to use to account for the runoff. If the layer has melted at the top snow or ice surface unconfined flow was used and if the layer has melted somewhere else in the snow or icepack confined flow was used. After the layer has melted the layer will not runoff until the runoff time is surpassed. The runoff time for unconfined flow was 11.28 s and 58 s for confined flow.

Using the Model's Main Interface

The main interface was developed to have few required inputs; this section will define the inputs required and how to use the interface. The first set of inputs includes the time of each step in seconds (dt), day of the year ($DOYR$), number of layers to be modeled (n_l), temperature of the ice/snow surface (T_{top}), and the number of time steps to be taken ($time_steps$). The next set of input data is used for display purposes. Because

the model uses matrices for all its calculations, when a layer has melted and runoff that layer must be removed from the matrix. When layers are removed the size of the matrix becomes smaller. To create history plots, each time step is saved into a larger matrix. To save the time step matrices into a large matrix each individual matrix needs to be the same size. This is the reason for having to specify meltall and the number of layers above the pavement to be saved (a_p). Meltall is a flag indicating whether or not the user expects all layers to melt. If one expects all the layers to melt, the flag would be set to "yes" or 1. If all the layers were not expected to melt then the flag would be set to "no" or 0. The number of layers above the pavement (a_p) to be saved in the large matrix is an input for the model when meltall is chosen to be "no" or 0. This command allows the user to see the time history temperatures of the layers that have not melted. For example, the model is run choosing meltall to be, yes; after the results are displayed one sees that there are seven remaining layers on the pavement. The user can then re-run the model choosing meltall, no, and a_p equal to 7 (Figure 13b), this will allow the user to see how the seven layers above the pavement surface changed temperature over the time period. Figure 13a is a sample of the codes flag settings where meltall is equal to yes and Figure 13b is where meltall is equal to no and a_p is equal to seven. Bold terms in Figure 13 refer to executable code. The last set of inputs for the model in the main is the layer properties, density, grain size, impurity content, and albedo.

```

a) %%% Important Question: Are you expecting all the layers to melt off?? %%
%% If the answer is yes then 'meltall = yes' if you don't expect it all %%
%% to melt choose meltall = no; Now specify how many layers you expect %%
%% to remain above the pavement surface (a_p) if one gets errors reduce %%
%% the a_p number. %%
%%
yes = 1;
no = 0;
meltall = yes;

a_p = 0; % how many layers above the pavement are to be saved and printed

if meltall == 1
    a_p = 0;
end

b) %%% Important Question: Are you expecting all the layers to melt off?? %%
%% If the answer is yes then 'meltall = yes' if you don't expect it all %%
%% to melt choose meltall = no; Now specify how many layers you expect %%
%% to remain above the pavement surface (a_p) if one gets errors reduce %%
%% the a_p number. %%
%%
yes = 1;
no = 0;
meltall = no;

a_p = 7; % how many layers above the pavement are to be saved and printed

if meltall == 1
    a_p = 0;
end

```

Figure 13. Sample code in the main program. (a) sample code for meltall = yes (b) sample code for metal = no and the a_p is defined.

Validation Experiment

Validation is a very important part of the modeling process. Without validation the accuracy of numerical models is unknown. A highway sub-grade box was constructed and bubble free ice was grown to try to validate the model. The box was built to simulate a typical highway cross-section. The box was 30 cm long, 30 cm wide, and 40 cm deep (Figure 14). Pinewood was used to build the frame of the validation box. 30 cm of the box was filled with unbound rock aggregate. A variation of the Marshall Method for

Bituminous Mix Design was used to create the bituminous asphalt used for the upper 10cm of the box. The aggregate was made in the asphalt-testing lab at Montana State University (MSU) with the typical amounts of coarse aggregate, fine aggregate, and sands. Aggregate was heated in an oven to 110° C as per the Marshall Method. The following formula was used to calculate the total weight (TW) of the aggregate and the asphalt [Montana 2000]

$$TW = \frac{AGW}{1 - \%asphalt}, \quad (79)$$

where AGW is the aggregate weight and $\%asphalt$ is the percent of asphalt required.

5.5% asphalt by weight was used, which is typical of a bituminous highway design [Huang 1993]. From the total weight, the weight of the asphalt was calculated and added to the aggregate. The aggregate and asphalt were mixed together then added to the box in 4 2.5 cm lifts, compacted 50 times using a compaction hammer. Figure 14 shows the box and the asphalt layer.

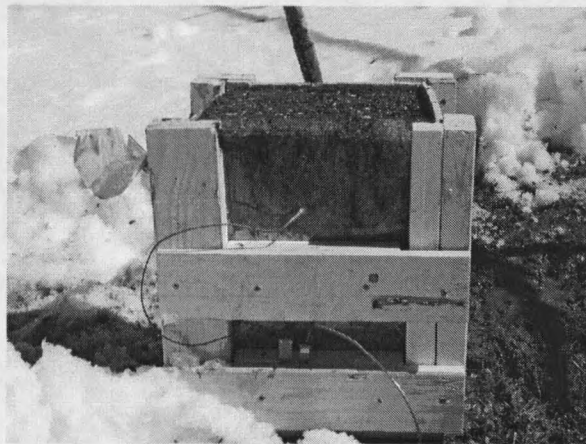


Figure 14. Test box used for the validation experiment.

Meteorological data was collected as input into the model and temperatures were measured from the box and the ice. The goal was to use the weather and solar inputs, run the model and forecast the temperatures that were measured and ice depths that were observed. Due to numerous uncontrollable variables such as (e.g., convection around the test box, angle of incoming solar radiation, shading from the solar radiation, varying cloud cover, runoff flow direction, and air temperature) the validation experiment was used only to match trends of the model's reactions to the input parameters, not exact temperatures and melting times.

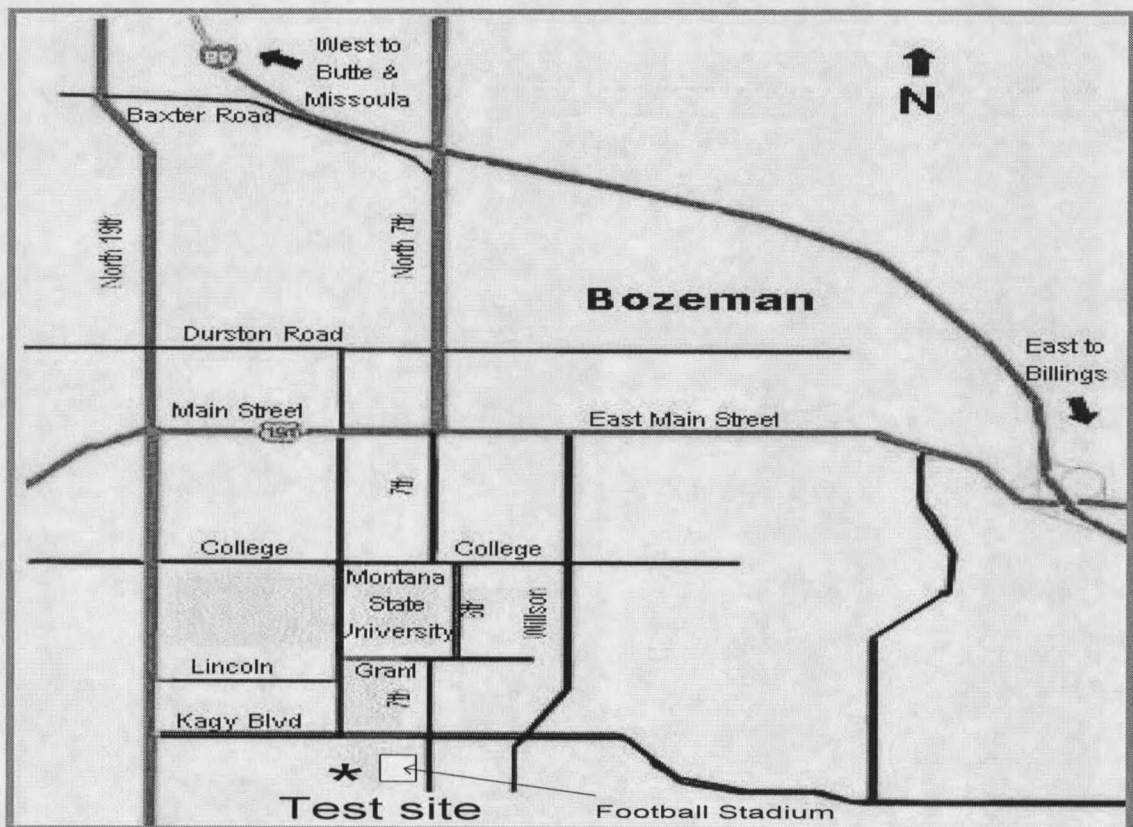


Figure 15. Map of Bozeman, MT and the location of the test site.

The location for the test site was southwest of the intersection at Kagy and 7th in a field next the MSU football stadium in Bozeman (Figure 15). A hole was dug 40 cm into the ground and the box was set in place with a 2-3° slope for runoff purposes. The box was placed in the ground days before the experiments took place, to reach steady state in the box. A plastic casing was placed around the ice, to hold the ice samples so the sample's flow was controlled to be in the direction of the downward slope. To try and reduce sample error, pure bubble free ice was used for all the test cases.

The pure bubble free ice was grown in the MSU cold regions laboratory using the following protocol. First the water was boiled for 2-3 hours to decrease the amount of dissolved gas in the water. Then, the water was cooled and poured slowly (reducing the mixing of air into the water) into container in the cold room, which was then sealed. The ambient room temperature was held at constant temperature of -10 °C. Water remained in the containers until the temperature of the water was cool, but not yet freezing. At this time the water was transferred into a large, approximately .5 m diameter, insulated bowl. As the water freezes at the surface, air is rejected from the interface and forced into the water below until the water becomes saturated leading to the formations of bubbles at the interface. After the water had completely frozen there was about a 12 cm layer of bubble free ice in the top of the insulated bowl (Figure 16). The bubble free ice was cut using a band saw into 20 x 20 cm sections with depths of 15 mm, 20 mm, 35 mm, and 40 mm and stored in the cold room until the time of the experiment.

To freeze the ice blocks to the asphalt test surface, the ice block was placed on the test surface while the temperatures were still below freezing. Water was sprayed in between the ice block and the asphalt surface until the ice block had frozen to the surface.

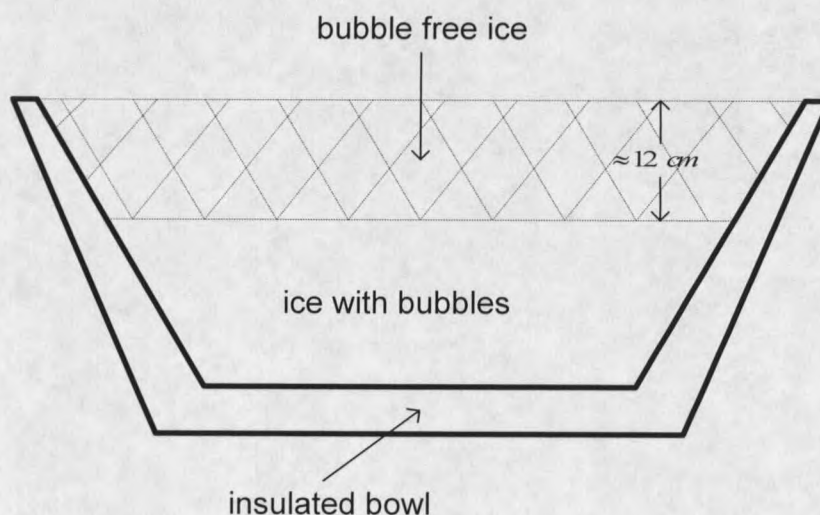


Figure 16. Drawing of the insulated bowl used when making pure ice.

Solar radiation, temperatures, relative humidity, barometric pressure, and wind speed were measured. With no instruments available, cloud cover was estimated by looking at the sky and making educated guesses regarding what fraction of the sky had cloud cover. These observations were made every hour. A Li-Cor LI-200SA pyranometer was used to measure the incoming solar radiation in W/m^2 . The Li-Cor pyranometer was calibrated during daylight to a highly accurate Eppley Precision Spectral Pyranometer (PSP) which has a uniform spectral response from 280 – 2800 nm. Under most natural daylight conditions, the error of Li-Cor LI-200SA is less than 5% [Li-Cor LI-200SA pamphlet]. Copper-constantan T-type thermocouples were used for temperature measurement. A

thermocouple uses the voltage difference caused by the connection of the two metals (copper and constantan for T-type) this voltage difference varies linearly with temperature, and once calibrated to a reference temperature, allows temperature to be measured [Omega 1989]. A total of six thermocouples were placed in the following locations: one 1 m into the ground to measure the diurnal depth temperature, one at the sand aggregate interface, one at the asphalt aggregate interface, one at the pavement ice interface, one at the ice surface, and one to measure air temperature. Air temperature was measured 20 cm and 3 m above the ice surface by a thermocouple, and the WEATHERPAK 400, respectively. A CR10 Campbell Scientific datalogger was used to collect the solar radiation data. Since the experiment called for more temperature readings than the CR10 had ports, a AM416 Campbell Scientific relay multiplexer was added to the CR10 to collect the necessary temperature data. The CR10 was programmed to take solar and temperature readings every minute during the experiment. A Costal Environmental Systems WEATHERPAK-400, along with its Intercept software (version 3.34b), was used to collect the air temperature ($^{\circ}\text{C}$), barometric pressure (mbar), relative humidity (%), and wind speed (m/s). The WEATHERPAK-400 is a portable weather station used for numerous applications. The WEATHERPAK-400's datalogger and software collected readings every 30 seconds. Figure 17 is a picture of the WEATHERPAK-400; the Li-Cor LI 200SA is attached.



Figure 17. Picture of the WEATHERPAK-400 and the Li-Cor pyranometer at the test site. [The Li-Cor pyranometer is mounted on the horizontal bar].

The model was run with the measured solar radiation, barometric pressure, wind speed, air temperature, relative humidity, and the observed cloud cover as inputs. The collected temperature data was graphed and compared to the model's output graphs. Due to the mild spring that southwest Montana experienced in 2002, only three experiments were performed. Chapter 4 presents the results of these experiments and other findings.

CHAPTER 4

FINDINGS/RESULTS

Ideal conditions for validating the numerical model occur with clear cool nights and a cool sunny day when the air temperature does not get much above 0° C. When air temperatures get above 0° C, melting will occur due to energy addition from convection and solar radiation. Test box construction, instrumentation, and programming for the validation experiment was not completed until the spring of 2002. Due to the mild spring of 2002 in southwest Montana, the area did not experience as many cool nights with sunny cool days, as was expected. The weather was either not cool enough to freeze the ice sample or the day was too warm. Due to weather conditions and technical difficulties, only three experiments were performed: April 02 2002, April 04 2002, and April 19 2002. This chapter presents the results from the three experiments, along with a set of hypothetical examples. Some of the examples include demonstrate how soot content may affect melting rates and the differences between how snow and ice absorb the solar radiation. Possible interpretations of the results, from the point of view of a winter maintenance forecaster, are also presented.

The Model and Experiments

This next section provides a comparison between results from both the model and the validation experiments. Adjusting the albedo, which the CAR provided, by 1 – 1.5% can play a large role in how well the model compares to the validation experiment. The

difference between the CAR albedos and the adjusted albedos will be presented for the April 19, 2002 experiment. For the other two experiments, adjusted albedos were used when comparing the experiment measurements to the models predictions.

April 19, 2002.

The night leading into the morning of April 19, 2002 was fairly cool, with average temperatures, from 12:00 am to 6:00 am, of -7°C . This subfreezing temperature made it possible to freeze an ice sample onto the test box. At 6:30 am, before sun rise, a 15 mm thick piece of bubble free ice was frozen to the test box, and data collection began. April 19, 2002 was a moderate day with temperatures in the morning and afternoon ranging from of -4 to -1°C and 0 to -3°C , respectively. Cloud cover was estimated to range from 20 to 50% during the test period, and maximum solar radiation was a little over 1000 W/m^2 . Figure 18b is a plot of the measured solar radiation (W/m^2) versus time (hr). Measured solar radiation may be a little high but it is not uncommon for this area to get solar radiation values above 1000 W/m^2 , this value was probably measured during a break in the cloud cover. According to Licor, manufacturer of the pyranometer for this experiment, 1000 W/m^2 is a high value of solar radiation expected to be measured on very sunny days and $150\text{-}250\text{ W/m}^2$ are values expected to be measured on days with 100% cloud cover [Li-Cor LI-200SA pamphlet]. At 10:25 am the ice block thickness was 11 mm and melting was occurring at the bottom, where the block was in contact with the asphalt. By 1:10 pm, all the ice had melted and the asphalt in the box was totally dry. At this time all the data acquisition equipment was turned off, after saving to a computer.

Input files for the model were created using air temperature, barometric pressure, relative humidity, and wind speed from the WEATHERPAK, solar radiation from the CR10, and cloud cover from observation. Temperatures collected through the test box were plotted in Excel and compared to modeled results. Figure 18a is a plot of all the temperatures ($^{\circ}\text{C}$) taken from the CR10: diurnal depth, aggregate sand interface, aggregate asphalt interface, asphalt surface, ice surface, and air temperature. For this case the temperature of interest was the asphalt/ice interface surface, because all the ice melted. In Figure 18a, the asphalt surface temperature has a thicker line weight than the others for ease of viewing. Model results using the input data from the experiment and albedos calculated from the CAR are shown below in Figure 19.

Figure 19a is a plot showing the diurnal swing in the temperature profile below the asphalt surface, a plot similar to Figure 19a was generated for every model run to show the different diurnal fluctuations. Figure 19b shows when the layers begin to melt off. At the beginning of the test the number of layers remains constant at 15. After 3.33 hours, the model indicates the melting of layers until 6 hours after the beginning, when all the layers have melted and runoff. The ice layers do not begin to melt off until the temperature of the asphalt ice interface is at zero degrees and the asphalt surface temperature does not begin to rise above zero degrees until all the ice has melted and runoff. Figure (b), the numbers of layers versus time, as displayed in Figure 19b, is provided with every model example. Comparing Figure 19c and the pavement temperatures from Figure 18, it seems that the model's pavement temperatures are following the same trend but lag by forty-five minutes.

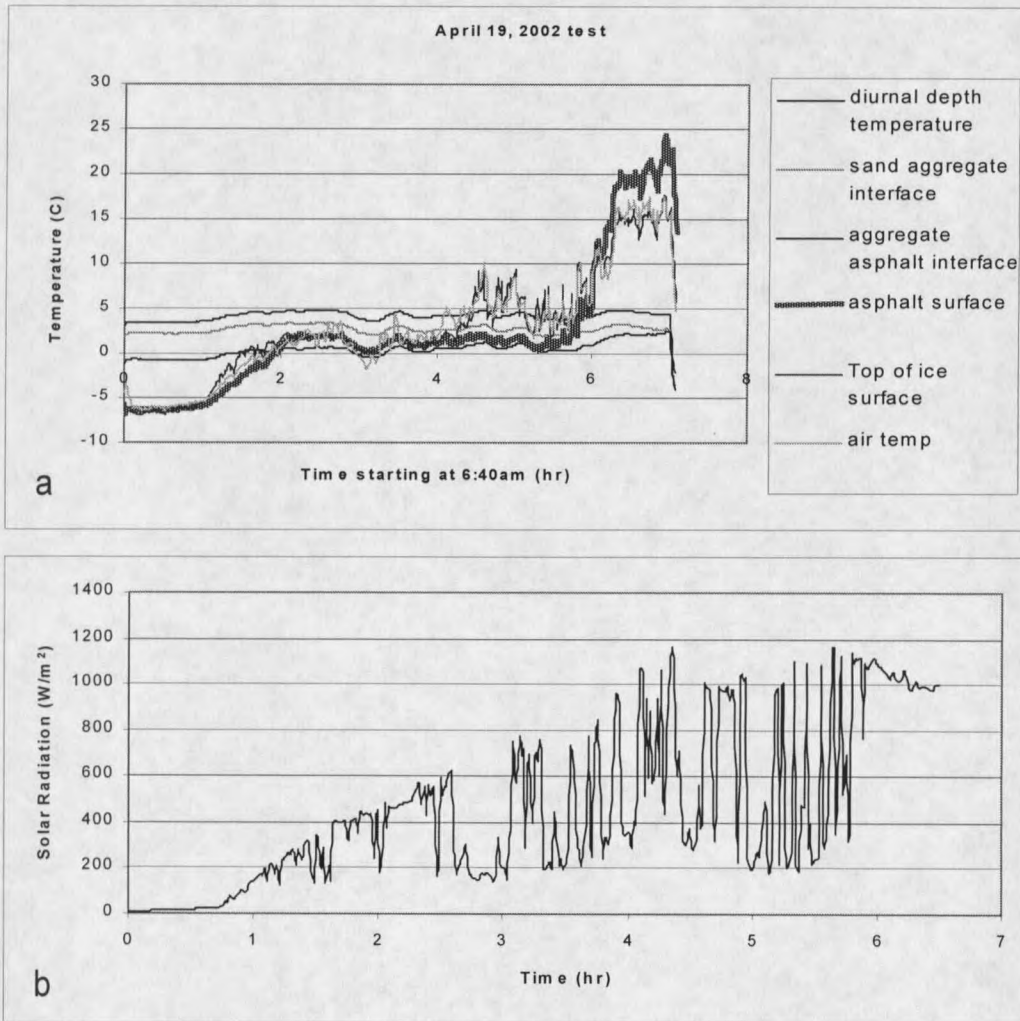


Figure 18. Plots created during the validation experiment on April 19, 2002. (a) temperature vs. time for six thermocouples used in the experiment. (b) measured solar radiation vs. time.

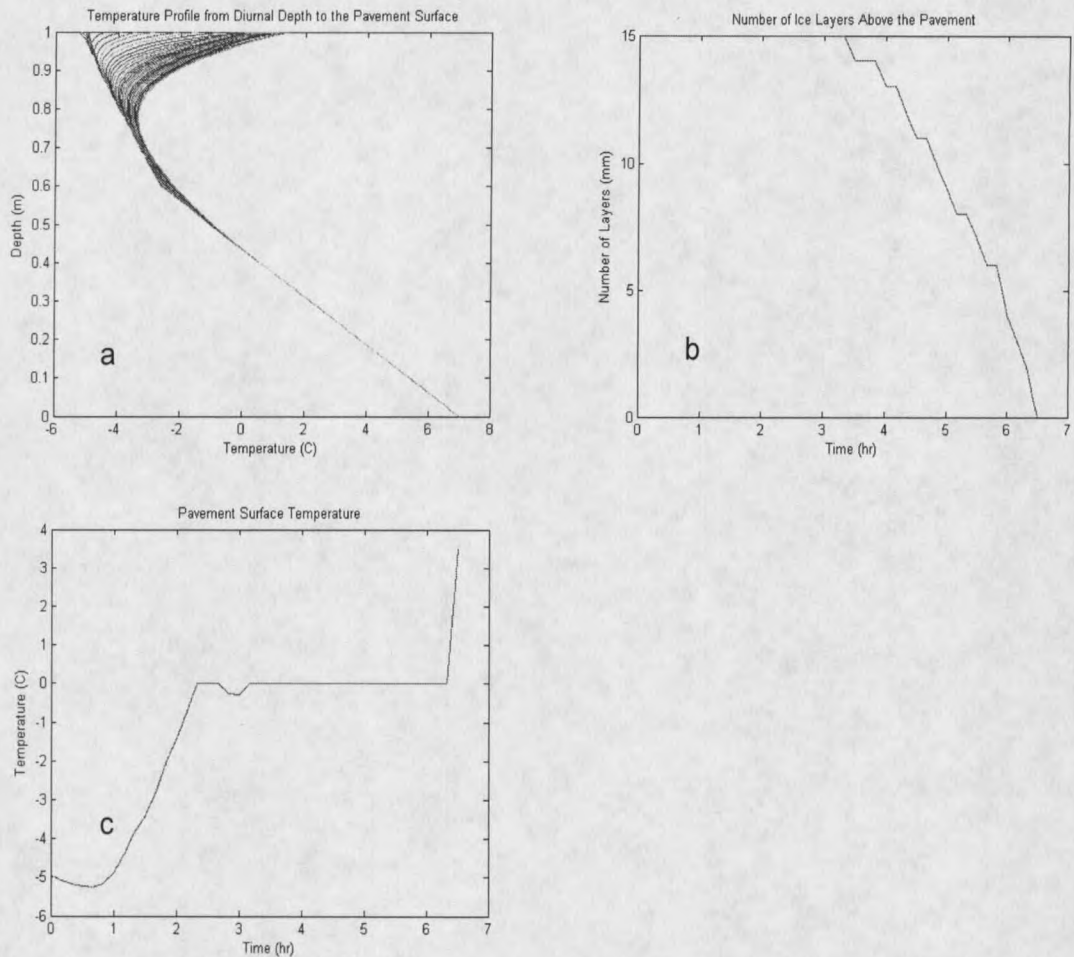


Figure 19. Model results for April 19, 2002. (a) sub-grade profile depth vs. temperature plotted every ten minutes. (b) number of ice layers vs. time. (c) pavement surface temperature vs. time.

Assuming that the lagging temperature response was a result of insufficient solar radiation to drive the heating rate of heating the asphalt surface, the albedos used in the model were reduced by 1%. By reducing the albedo more solar radiation was allowed to penetrate to the asphalt surface, heating the surface faster. Table 5 displays the albedos for each layer with CAR produced, generated albedos in column 1, and the reduced

albedos in column 2. Figure 20 displays the model results using the reduced albedos. A total albedo was calculated for each case. Total albedo represents the albedo for every layer combined along with the underlying surface. Total albedo, α_{total} , is calculated using the following equation:

$$\alpha_{total} = \frac{(I_o - I_{tot_a})}{I_o}, \quad (80)$$

where, I_o is the initial solar radiation at the surface and I_{tot_a} is the summation of all the absorbed solar radiations in the ice/snow layers. Total albedo for the April 19 2002 with the reduced albedos, was calculated to be 51.9%.

Table 5. The albedo's for each layer that CAR generated and the adjusted albedo's used for generating results in Figure 20.

	CAR Albedo's	adjusted Albedo's
Layer 15	0.04	0.03
Layer 14	0.04	0.03
Layer 13	0.04	0.03
Layer 12	0.04	0.03
Layer 11	0.045	0.035
Layer 10	0.045	0.035
Layer 9	0.045	0.035
Layer 8	0.045	0.035
Layer 7	0.045	0.035
Layer 6	0.045	0.035
Layer 5	0.05	0.04
Layer 4	0.05	0.04
Layer 3	0.06	0.05
Layer 2	0.07	0.06
Layer 1	0.09	0.08
Asphalt	0.12	0.12

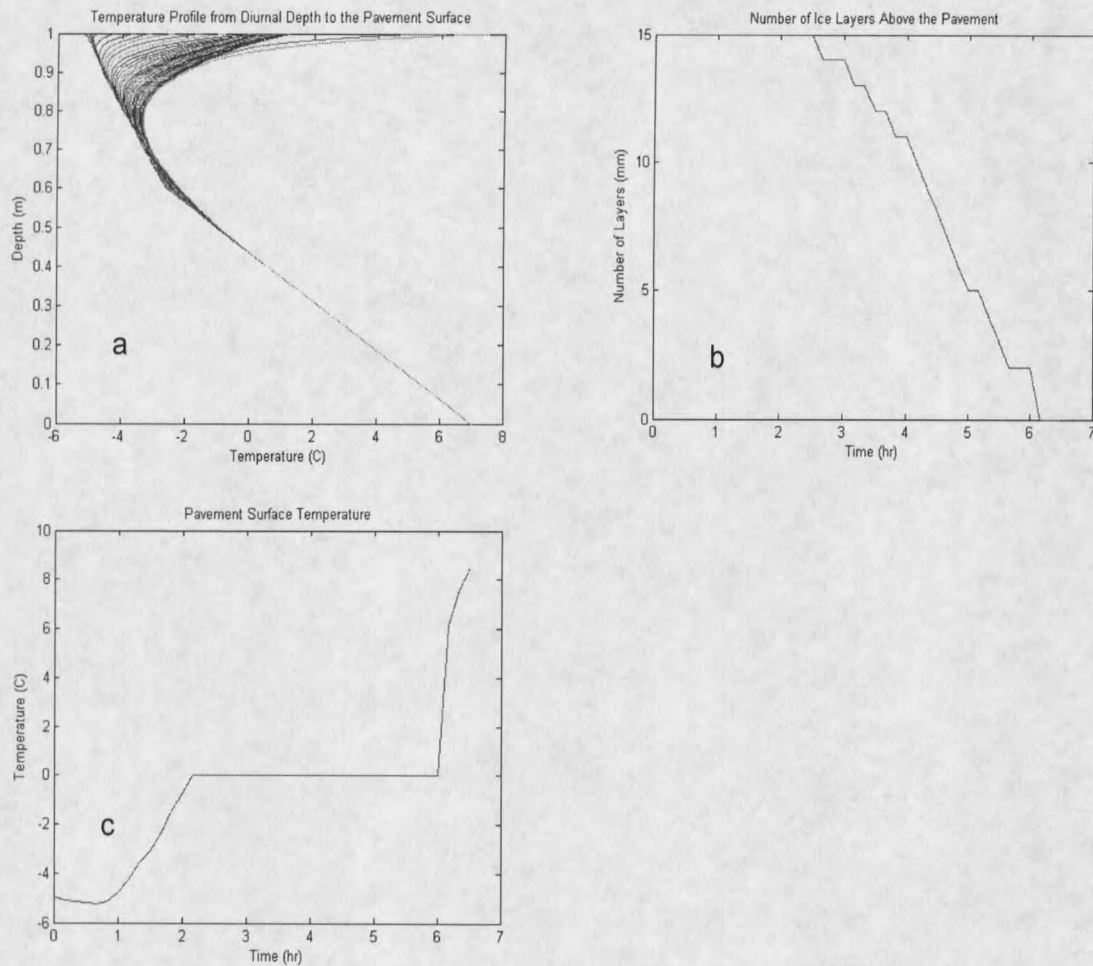


Figure 20. Model results for April 19, 2002 with adjusted albedo's. (a) sub-grade profile depth vs. temperature plotted every ten minutes. (b) number of layers vs. time. (c) pavement surface temperature vs. time.

Measured temperatures below the asphalt surface, shown in Figure 18, do not show good agreement with the modeled values displayed in either Figure 19a or 20a. However, both support the observation that the deeper into the ground the less temperature fluctuation there will be. Figure 20c shows that the model forecast an initial

pavement temperature of -5°C ; at 2 hours the pavement temperature heated enough to start changing the phase of the ice. The pavement surface stayed at 0°C until all the ice had melted and runoff, at 6.16 hours. Finally, the pavement temperature starts to heat up because there was no ice left on the surface. The measured asphalt surface temperatures from the experiment, Figure 18, follow the same pattern. The initial temperature of the asphalt surface is -6°C and increases for 2 hours until melting begins. The measured pavement temperature stays constant between 1 and 2°C during the phase change. After all the ice has melted and runoff, 5.75 hours, the surface temperature begins to rise. Figure 21, provides a comparison between the pavement temperature from Figure 18 and Figure 20c. Although, the beginning and ending temperatures do not match up, the time until phase change occurs and the time for all the ice to melt and runoff are almost exact. Figure 22, is a table with the measured ice thickness during the experiment along with a plot of both the measured ice thickness and the model's predicted ice thickness, Figure 20b, versus time.

Possible reasons for the temperature differences are provided in the following statements. When the test box was placed into the ground a hole 40 cm deep with an area of 3600 cm^2 was dug. The diurnal temperature thermocouple was placed another 60 cm below the hole and the other sub-grade thermocouples were placed inside the box. A major source for error in the sub-grade temperatures comes from the convection around the box and in the hole causing sub-grade temperatures to be cooler than expected. Another source for error in the experiment was the visible thermocouples. The copper-constantan thermocouples have higher absorptive properties than pure ice causing the

thermocouple to heat faster from the short-wave radiation than the ice, therefore recording inaccurately high temperatures.

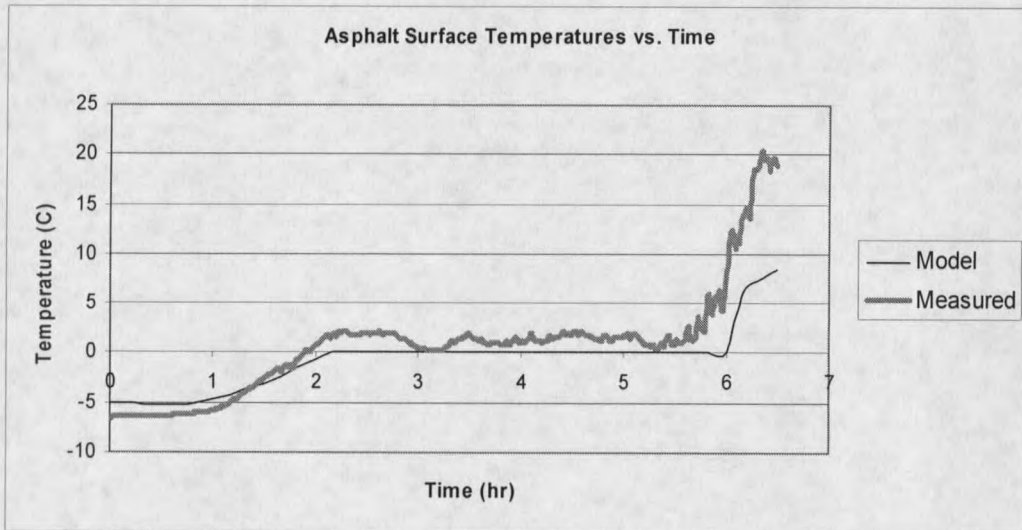


Figure 21. Plots of both the measured and the model's predicted asphalt surface temperature vs. time for the April 19, 2002 experiment.

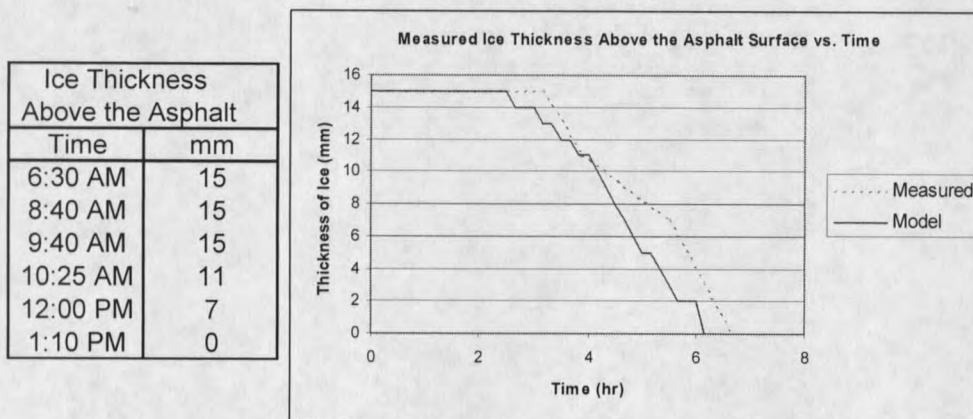


Figure 22. Values of measured thickness of ice above the asphalt surface during the experiment, and a plot of both measured and predicted thickness of ice above the asphalt surface vs. time for the April 19, 2002 experiment.

